Large-eddy simulation of interacting barchan dunes in a steady, unidirectional flow.

Mohammad Omidyeganeh,[1] Ugo Piomelli,[1] Kenneth T. Christensen,[2] and James L. Best[2,3]

[1]Department of Mechanical Engineering and Materials, Queen's University, Kingston, Ontario, Canada.

[2]Department of Mechanical Science and Engineering, University of Illinois, Urbana-Champaign, Illinois, USA.

[3]Departments of Geology, Geography and Geographic Information Science and Ven Te Chow Hydrosystems Laboratory, University of Illinois, Urbana-Champaign, Illinois, USA.

Abstract. We have performed large-eddy simulations of turbulent flow over barchan dunes in a channel with different interdune spacings in the downstream direction at Reynolds number, $Re_\infty \simeq 26000$ (based on the free stream velocity and channel height). Simulations are validated against experimental data (at $Re_\infty = 55460$); the largest interdune spacing (2.38λ, where λ is the length of the barchan model) presents similar characteristics to the isolated dune in the experiment, indicating that at this distance the sheltering effect of the upstream dune is rather weak. We examine 3D realizations of the mean and instantaneous flow to explain features of the flow field relevant to sediment transport. Barchan dunes induce two counter-rotating streamwise vortices, along each of the horns, which direct high-momentum fluid toward the symmetry plane and low-momentum fluid near the bed away from the centerline. The flow near the bed, upstream of the dune, diverges from the centerline plane, decelerates and then rises on the stoss side of the dune while accelerating; the flow close to the centerline plane separates at the crest and reattaches on the bed. Away from the centerline plane and along the horns, flow separation occurs intermittently. The flow in the separation bubble is routed towards the horns and leaves the dune at their tips. The separated flow at the crest reattaches on the bed, except on the centerline symmetry plane of the dune, where a weak saddle point of separation appears at the bed. The distribution of the bed shear-stress, characteristics of the separation and reattachment regions, and instantaneous wall turbulence are discussed. Characteristics of the internal boundary layer developing on

the bed after the reattachment region are studied. The interdune spacing is found to affect significantly the turbulent flow over the stoss side of the downstream dunes; at smaller interdune-spacings, coherent high- and low- speed streaks are shorter but stronger, and the spanwise normal Reynolds stress is larger. The turbulent kinetic energy budgets show the importance of the pressure transport and mean-flow advection in transporting energy from the overlying wake layer to the internal boundary layer over the stoss side of the closely-spaced dunes. The characteristics of the separated-shear layer are altered slightly at smaller interdune spacing; the separation bubble is smaller, the separated-shear layer is stronger, and the bed shear-stress is larger. Away from the dunes, typical wall-turbulence structures are observed, but coherent eddies generated in the separated-shear layer due to the Kelvin-Helmholtz instability are dominant near the dune. Coherent structures are generated more frequently at smaller interdune spacing; they move farther away from the bed, towards the free surface, and remain in between the horns. At larger interdune spacings, these coherent structures are advected in the spanwise direction with the mean streamwise vortices and can be observed outside of the dunes.

1. Introduction

The interaction of turbulent flow with a mobile sand bed, when the flow is unidirectional and sand supply is limited, results in the formation of barchan dunes in aeolian, marine and fluvial environments. Barchans have a planform crescentic topography with horns elongated in the downstream direction [*Kroy et al.*, 2005], and are extensively observed in deserts on Earth [*Bagnold*, 1941; *Lancaster*, 1995], and on Mars [*Breed et al.*, 1979], but more rarely in rivers and the oceans [*McCullogh and Janda*, 1964; *Allen*, 1968]. The linear relationship between the width of the dune, its height and wavelength and its three-dimensional shape are well understood [*Hesp and Hastings*, 1998]. Barchans rarely exist as isolated forms and may occur in large fields [*Hersen et al.*, 2004] up to several hundred square kilometers in area [*Lettau and Lettau*, 1969]. The sediment transport associated with barchan dunes has attracted many researchers to study their fluid and morphological dynamics in many differing environments with barchans.

The complexity of the three-way coupling between bedform, fluid flow, and sediment transport can be simplified by considering one or two of these mechanisms in isolation and then extracting their influence on the others [*Best*, 2005]. This simplification is justified knowing that sediment transport occurs at smaller spatio-temporal scales than the energetic flow scales, and that these are smaller than the scales of bedform deformation and interaction [*Hersen et al.*, 2004].

After the early work by *Bagnold* [1941], the geomorphology of sand dunes has been studied and discussed in review papers by *Andreotti et al.* [2002] and *Livingstone et al.* [2007]. A body of research has been devoted to small-scale grain transport mechanisms over

flat surfaces [*Andreotti et al.*, 2002] and sloping bedforms considering the changes in the threshold of sediment transport [*Hardisty and Whitehouse*, 1988; *Iversen and Rasmussen*, 1994]. Other research has studied the large-scale dynamics of dunes by examining their dimensions [*Hesp and Hastings*, 1998] and interactions within dune fields [*Breed et al.*, 1979], both experimentally [*Endo et al.*, 2004], or by modelling sand transport in a large domain and predicting an equilibrium state for their size and arrangement [*Lima et al.*, 2002].

Models for solitary dunes cannot describe the steady state of barchan dune fields [*Hersen et al.*, 2004]; dunes receive sediment on their stoss side, and lose sediment through their horns; hence large dunes grow and move slowly while small dunes shrink and move faster. Additionally, based on the models in literature, the length scales required for the instability of deformation are much smaller than the dune sizes found in nature [*Hersen et al.*, 2004]; hence, there must be yet unknown physics that keep dune fields steady and determine the interdune spacing.

Most measurements and calculations of flow and sediment transport have been performed on the streamwise-wall-normal symmetry plane of barchans, especially over the windward stoss side [*Lancaster*, 1985; *Walmsley and Howard*, 1985; *Lancaster et al.*, 1996; *Wiggs et al.*, 1996; *McKenna Neuman et al.*, 2000; *Palmer et al.*, 2012]. Theoretical efforts have also usually considered transverse dunes [*Lancaster*, 1985; *Walmsley and Howard*, 1985; *Frank and Kocurek*, 1996; *Lancaster et al.*, 1996; *Wiggs et al.*, 1996; *McKenna Neuman et al.*, 2000] and adapted an extended version of boundary layer theory [*Schlichting*, 1955] to the flow over gently sloping symmetrical hills [*Jackson and Hunt*, 1975]. However, the velocity profiles do not often obey the logarithmic law-of-the-wall over barchan dunes

[*Frank and Kocurek*, 1996; *Wiggs et al.*, 1996; *McKenna Neuman et al.*, 2000]. Early numerial experiments on the development and migration of an isolated dune by *Wippermann and Gross* [1986] assumed log-linear behavior and could just explain the sensitivity of the wind speed on the shape of barchan dunes, similar to the picture presented by *Bagnold* [1941], *Finkel* [1959] and *Allen* [1968].

Advanced analysis of flow characteristics has often been performed over transverse dunes [*Frank and Kocurek*, 1996; *McKenna Neuman et al.*, 2000]. Some theoretical efforts [*Frank and Kocurek*, 1996] explained the shear layers over the lee side of aeolian dunes and development of a thin internal boundary layer downstream of the flow reattachment region. The intermittent behavior of turbulence structures and sediment transport was studied by *McKenna Neuman et al.* [2000] who studied the frequency spectra of streamwise velocity fluctuations and sediment transport over trasverse dunes. At low wind speeds, close to the sediment transport threshold, the intermittent nature of flow structures on sediment transport was found to be as important as the mean flow. *McKenna Neuman et al.* [2000] concluded that mean velocity is not a good indicator of sediment transport mechanisms at low wind speeds. The secondary flow over the lee side of transverse dunes has been studied by *Walker and Nickling* [2002, 2003]; grainfall transport and deposition is strongly linked with the vertical flow within the shear layer bounding the circulation bubble in the wake. The reversed flow in the recirculation cell was found to be strong enough to return sediment to the lee side of the dune [*Walker and Nickling*, 2003].

An interesting and yet ambiguous phenomenon in the morphology of barchan and transverse dunes is the sediment transport mechanism upstream of the toe of the dune, where the mean bed shear-stress decreases but, contrary to the expectation of sediment depo-

sition in this area, the transport rate does not decrease. Researchers conjecture that turbulence structures are responsible for sediment transport in this region [*Wiggs et al.*, 1996; *McKenna Neuman et al.*, 2000; *Walker and Nickling*, 2002, 2003; *Parsons et al.*, 2004a; *Weaver and Wiggs*, 2011]. The majority of sand transported is due to long-lasting positive wind fluctuations, while the influence of short time-scale events on the sediment transport is not yet understood. The concave curvature of streamlines was assumed to be responsible for the increase in Reynolds shear stresses [*Wiggs et al.*, 1996], with high-momentum structures being transferred to the low-momentum area near the bed, which increases the instability and hence the stress.

On the upper half of the stoss side, the bedform curvature changes from concave to convex, which stabilizes the flow that is also accelerated; these two mechanisms have opposing effects on sediment transport, with acceleration often overcoming the effects of curvature [*Weaver and Wiggs*, 2011]. A third zone exists if the dune crest does not coincide with the brink; flow decelerates after the crest towards the brink that, together with the convex curvature, cause deposition of sand [*Wiggs et al.*, 1996]. The dune profile (crest-brink separated or crest-brink coincident) thus affects the lee side flow characteristics [*Baddock et al.*, 2011]. While an increase in Reynolds shear stress and the streamwise component of stress can explain the maintenance of sand flux at the toe, further downstream, on the stoss side and near the crest, flow acceleration plays a more significant role [*Walker and Nickling*, 2003; *Weaver and Wiggs*, 2011]. A more sophisticated study is required to clarify the effects of acceleration and streamline curvature on the turbulence statistics and their budgets.

Several numerical studies have been conducted concerning flow over three-dimensional barchan dunes [*Wippermann and Gross*, 1986; *Takahashi et al.*, 1998]; they generally suffer from low grid resolution and inaccurate models. Reynolds-averaged Navier-Stokes solvers in 2D [*Parsons et al.*, 2004a, b] and 3D [*Hermann et al.*, 2005] provide mean-flow characteristics (flow acceleration/deceleration, separation, reattachment, and reversal) with qualitative agreement with the literature, but neglect the mean-flow three-dimensionality and do not provide information on the instantaneous flow structures observed in experiments [*McKenna Neuman et al.*, 2000; *Franklin and Charru*, 2011] and their importance; e.g., elongated sand streaks observed on the stoss side of dunes, which indicate significant contributions of wall turbulence to sediment transport [*Franklin and Charru*, 2011; *Charru and Franklin*, 2012].

The effects of interdune spacing on dune dynamics have been largely ignored, despite the fact that the spacing affects the flow on the lee side of the upstream dune and the stoss side of the downstream bedform [*Fernandez et al.*, 2006], and may change the mechanisms of sediment transport, which are assumed to depend on the spacing and dune sizes [*Walker and Nickling*, 2003; *Baddock et al.*, 2007; *Palmer et al.*, 2012]. The importance of the secondary flows observed in the lee side on intermittent sediment transport over the stoss side of the downstream dune was studied by *Walker and Nickling* [2003]; high variability in bed shear-stress in the reattachment zone inhibits sediment deposition and can cause deformation of the stoss side of the downstream dune. At interdune spacings close to the size of the separation zone, regular deformation models [*McLean and Smith*, 1986] cannot explain the physics, even for transverse dunes [*Baddock et al.*, 2007]. *Palmer et al.* [2012] conducted a series of novel experiments on the effects of interdune spacing on the

features of the separated shear-layer, separation-bubble size and approaching turbulence structures on the stoss side of the downstream dune. The sheltering effect of the upstream dune on the flow over the downstream dune, in which the vortices formed on the separation zone shear layer were advected downstream and transported energy to smaller scales, was identified.

The process of interaction between barchan dunes has been studied in aeolian [*Kocurek et al.*, 2010] and aqueous [*Endo et al.*, 2004] environments. In water flows, *Endo et al.* [2004] observed three types of interaction occurring as the volumetric ratio between the two adjacent bedforms increased: (1) absorption, (2) ejection, and (3) splitting. *Kocurek et al.* [2010] supported the hypothesis that interactions emerge from bedform-level sediment transport in a hierarchy that includes grain-fluid interactions and dune-dune interactions.

However, all efforts to date lack an accurate representation of the bed shear-stress, which provides insight on the sediment transport mechanisms in a three-dimensional view. Turbulent flow over the lee side of the dune, where the flow separates at the crest and broad ranges of length- and time-scales are introduced into the turbulence spectrum, is poorly understood. This situation is even more complicated as the flow separates intermittently on the horns of the dune and, on some parts of the crestline, it is oblique with respect to the crestline. Additionally, the three-dimensional characteristics of mean flow and turbulence have yet to be studied with a reasonable resolution. The significant effect of interdune spacing on the mean-flow and instantaneous flow features have also yet to be examined in detail. In this paper, we present a series of resolved large-eddy simulations of flow over a model barchan dune similar to that studied experimentally by *Palmer et al.* [2012] at various interdune spacings, to obtain a more comprehensive understanding of

the 3D mean flow characteristics and turbulence coherent structures at differing dune spacings.

2. Problem formulation

In large-eddy simulations, the velocity field is separated into a resolved (large-scale) and a subgrid (small-scale) field, by a spatial filtering operation [*Leonard*, 1974]. The non-dimensionalized continuity and Navier-Stokes equations for the resolved velocity field are

$$\frac{\partial \overline{u}_i}{\partial x_i} = 0, \tag{1}$$

$$\frac{\partial \overline{u}_i}{\partial t} + \frac{\partial \overline{u}_i \overline{u}_j}{\partial x_j} = -\frac{\partial \overline{P}}{\partial x_i} - \frac{\partial \tau_{ij}}{\partial x_j} + \frac{1}{Re_\infty}\nabla^2 \overline{u}_i + f_i \delta_{i,1}, \tag{2}$$

where $Re_\infty = U_\infty h/\nu$, h is the channel height, and U_∞ is the free-stream velocity over the toe of the dune. We use U_∞ for the normalization of the statistics throughout the paper. x_1, x_2 and x_3 are the streamwise, vertical and spanwise directions, also referred to as x, y and z. The velocity components in these directions are, respectively, u_1, u_2 and u_3 (or u, v and w). An overline denotes a filtered quantity, and $\tau_{ij} = \overline{u_i u_j} - \overline{u}_i \overline{u}_j$ are the subgrid stresses, which were modeled using an eddy-viscosity assumption

$$\tau_{ij} - \delta_{ij}\tau_{kk}/3 = -2\nu_T \overline{S}_{ij} = -2C\overline{\Delta}^2 |\overline{S}| \overline{S}_{ij}. \tag{3}$$

Here, $\overline{\Delta} = 2\left(\Delta x \Delta y \Delta z\right)^{1/3}$ is the filter size, $\overline{S}_{ij} = \left(\partial \overline{u}_i/\partial x_j + \partial \overline{u}_j/\partial x_i\right)/2$ is the resolved strain-rate tensor and $|\overline{S}| = \left(2\overline{S}_{ij}\overline{S}_{ij}\right)^{1/2}$ is its magnitude. The coefficient C is determined using the dynamic model [*Germano et al.*, 1991] with the Lagrangian averaging technique proposed by *Meneveau et al.* [1996], and extended to non-Cartesian geometries by *Jordan* [1999] and *Armenio and Piomelli* [2000]. The flow is driven by a mean pressure gradient, f_i, which is determined at each time step to ensure a fixed flow rate through the channel.

The governing differential equations (1) and (2) are discretized on a non-staggered grid using a curvilinear finite-volume code. The method of *Rhie and Chow* [1983] is used to avoid pressure oscillations. Both convective and diffusive fluxes are approximated by second-order central differences. A second-order-accurate semi-implicit fractional-step procedure [*Kim and Moin*, 1985] is used for the temporal discretization. The Crank-Nicolson scheme is used for the wall-normal diffusive terms, and the Adams-Bashforth scheme for all the other terms. Fourier transforms are used to reduce the three-dimensional Poisson equation into a series of two-dimensional Helmholtz equations in wave-number space, which are solved iteratively using the BiConjugate Gradient Stabilized method. The code is parallelized using the Message-Passing Interface and the domain-decomposition technique, which have been extensively tested for turbulent flows [*Silva Lopes and Palma*, 2002; *Silva Lopes et al.*, 2006; *Radhakrishnan et al.*, 2006, 2008; *Omidyeganeh and Piomelli*, 2011].

The barchan dune (Figure 1) was generated from the model used in the experiments of *Palmer et al.* [2012] that reflects the typical shape of barchans in nature [*Hersen et al.*, 2004]. The aspect ratio of the current model falls in the range of laboratory and field measurements [*Palmer et al.*, 2012]. The barchan model has a length of $\lambda = 3.62h$, width of $W = 3.62h$, and height of $H = 0.135h$. The ratio of the dune height, H, to the channel height, h, is equal to the ratio of the dune height to the boundary layer thickness in the experiment [*Palmer et al.*, 2012]. The simulation adopts an immersed boundary method based on the volume of fluid (VOF) technique [*Hirt and Nicholas*, 1981] to model the barchan. On the bed, the no-slip boundary condition is used, and periodic boundary conditions are employed in the streamwise (x) and spanwise (z) directions. The top

surface is assumed to be rigid and free of shear stress: the vertical velocity is set to zero there, as are the vertical derivatives of the streamwise and spanwise velocity components. The Reynolds number ranged between $25900 \leq Re_\infty \leq 26640$ for different simulations and is less than half that of the experiments of *Palmer et al.* [2012] ($Re_\infty = 55460$).

A series of simulations was conducted to study the effects of interdune spacing on the physics of the flow (Table 1). A Cartesian mesh was generated, with the grid distribution in the wall-normal direction being uniform up to the highest point of the dune, and then stretched by a hyperbolic tangent function. The grid in the spanwise direction was uniform, while in the streamwise direction a higher resolution was used over the lee side of the dunes, since the bed slope is significant in this zone and the flow separates. For all cases mentioned in Table 1, the grid distribution was the same. We performed a grid refinement study for Case 1 with a focus on the resolution of the VOF model over the lee side of the dune, as well as the convergence of statistics. Three simulations with $64 \times 158 \times 128$, $128 \times 158 \times 256$, and $160 \times 281 \times 512$ grid points were examined, with the two finest simulations producing grid-converged results with resolution $\Delta x^+ < 28.86$, $\Delta y^+ < 0.83$, and $\Delta z^+ < 10.55$, where the plus sign in the superscript represents normalization with respect to the local bed shear-velocity u_τ and kinematic viscosity ν. First- and second-order statistics were within 5% of each other for all resolutions. Only the results obtained with the finest grid resolution are shown herein. Note that the grid spacings above are comparable to those used in many Direct Numerical Simulations of the Navier-Stokes equations.

The equations were integrated for $900H/U_\infty$ time units to remove transient effects, and then statistics were accumulated over $1200H/U_\infty$ time units. To increase the sample size,

averaging was also performed over the symmetric points in the spanwise direction. To verify the adequacy of the sample, we compared statistics obtained using only half of the sample with those obtained using the complete sample, and found that the mean velocities differed by less than 3%, and the root-mean-square (rms) intensities by less than 7%.

3. Results

The present model has been extensively validated in three-dimensional flows with separation, [*Radhakrishnan et al.*, 2006, 2008], and over dunes in particular [*Omidyeganeh and Piomelli*, 2011, 2013]. *Omidyeganeh and Piomelli* [2011] performed extensive quantitative comparisons of the LES model (carried out with the present code and with similar parameters and grid spacings) with experiments and other simulations for the flow over 2D dunes, obtaining excellent agreement with the reference data with grid spacings similar to the present; the extension to 3D dunes [*Omidyeganeh and Piomelli*, 2013] showed that the main features of the flow are also captured well for highly three-dimensional mean flows. In the present work, comparison of the numerical model with the experiments [*Palmer et al.*, 2012] is difficult because of substantial differences between experimental and numerical configurations. First of all, the periodic condition in the horizontal directions used in the present model implies that we simulate the fully developed flow over an infinite array of dunes, uniformly distributed in the streamwise and spanwise directions. The experiments [*Palmer et al.*, 2012], on the other hand, considered either an isolated dune, or two barchans in tandem with zero streamwise spacing. Secondly, the experiment was carried out in a boundary layer, while in the simulation, since periodic boundary conditions were used, no boundary layer growth was allowed, and the top boundary of the domain was a line of symmetry; the lack of entrainment (or detrainment) thus alters the acceleration (or

deceleration) that the mean flow experiences, and may also affect some turbulence quantities. Finally, and most importantly, the Reynolds number in the experiment is over twice that of the numerical simulation. Since the number of grid points required by a resolved LES scales with $Re^{37/14}$ [*Choi and Moin*, 2012], the extra computational cost required by a calculation that matched the experiment would have made this study infeasible. Despite these differences, the agreement is qualitatively and quantitatively good, as will be shown below. In the following, we first compare the numerical results with the experimental data that are available only for the symmetry plane; then, we stress the three-dimensional features of the mean flow. Finally, we examine instantaneous flow visualizations to highlight the effects of the dune configuration on the turbulence structure.

3.1. Statistics in the symmetry plane

Mean streamwise velocity contours and streamlines are shown for experiments [*Palmer et al.*, 2012] and simulations in Figure 2. We chose Cases 1 and 5, which more closely resemble the experimental configurations: Case 5, which has the largest interdune spacing is found to be similar to the isolated dune case, while Case 1 is similar to the case in which measurements were taken over the second dune in an array with zero streamwise spacing. An important difference between experimental and numerical results is the higher velocity observed over the crest in the simulations, compared to the experiments. Two reasons contribute to this behavior: the additional blockage in the open channel (compared with the boundary layer), and secondary flows that are observed in the simulation, and which will be discussed later. The flow separates at the crest and reattaches on the bed at $x_r/H \simeq 4.5 - 5.6$. The predicted reattachment length is slightly larger than in the experiments, perhaps because of the higher velocity over the crest predicted by the

simulations. In the zero-spacing cases (Figure 2*(c,d)*), the reattachment length decreases further (compared to the isolated dune case) because of the bed-ward motion upstream of the dunes, reflected by the streamline curvature at $x/H < -8.0$.

A comparison of the Reynolds shear stress between simulations and experiments (Figure 3) reveals the contribution of the upstream dune on the flow over the downstream barchan when the dunes are close to each other. Although the separated shear layer is stronger in the simulations due to the higher speed (and velocity gradient, $\partial\langle\overline{u}\rangle/\partial y$), the extension of the shear layer towards the downstream dune agrees with the experiment. We also observe good agreement between the case with the largest spacing and the isolated dune of the experiment, indicating that, by 2.38λ, the sheltering effect of the upstream dune on the downstream barchan has become small.

Velocity and Reynolds stresses are also shown in Figure 4, in which profiles are compared at three locations: upstream of the dune ($x/H = -9.0$), at the crest ($x/H = 0.0$), and over the lee side of the dune ($x/H = 2.0$). The freestream velocity at the toe of the dune is used for normalization of the data. The behavior of the velocity profiles is similar to the experiments [*Palmer et al.*, 2012], despite some differences that can be attributed to the Reynolds number (the experimental profiles being fuller for instance). For the zero-spacing case, the effect of the upstream dune is reflected in a two-layer structure of the mean velocity, in which the wake with higher momentum overlies the internal boundary layer at the bed; this results in an inflectional velocity profile. The inherent instability of the inflectional profile results in higher levels of plane turbulent kinetic energy, $q_s^2 = (\langle u'u'\rangle + \langle v'v'\rangle)/2$, and primary Reynolds shear stress, $-\langle u'v'\rangle/U_\infty^2$. On the other hand, the isolated case shows a single layer, similar to a boundary layer profile,

and also to the largest interdune-spacing LES (Case 5). The two-layer profiles are still observed over the crest (Figure 4*(b)*) but have disappeared over the lee side (Figure 4*(c)*).

The profiles of Reynolds stresses also show good agreement with the experiments. Two peaks in the vertical profile of the turbulent kinetic energy, Figures 4*(e)* and *(f)*, for Case 1 represent two shear layers, with the overlying one being weaker. At the crest (Figure 4*(e)*), there is a near-bed peak representing the developing boundary layer on the stoss side for both simulations, and a second peak at $y/H \simeq 2.0$ for the zero-spacing case due to the upstream dune. Over the lee side (Figure 4*(f)*), the outer-layer peak can still be observed at $y/H \simeq 2.5$, while all cases show significant turbulent kinetic energy in the separated-shear layer. Upstream of the dunes, Figure 4*(d)*, the internal boundary layer on the bed has a single peak, while the zero-spacing case has a second (outer) one due to the separated-shear layer coming from upstream. The primary Reynolds shear stresses (Figures 4*(g-i)*) are also more significant in the separated-shear layer, compared to the developing boundary layer; at the crest, the peak of the profiles near the bed has disappeared due to the acceleration of flow on the stoss side, which dampens the turbulence near the bed [*Weaver and Wiggs*, 2011]. This behavior will be examined further later.

After flow reattachment, the flow on the centerline exhibits a region in which the pressure gradient is nearly zero; this zone extends, for Case 5, from $x/H \simeq -49.5$ to -14.0, for a total length of $35.5H$. The velocity profiles in wall units on four vertical lines along this region are shown in Figure 5. The profiles approach the log-law from below, and at the end of the zero pressure gradient zone they show a region of logarithmic behavior. The boundary-layer recovery is faster at the beginning of the zero-pressure region, and becomes significantly slower from $x/H = -30.0$ to $x/H = -14$. Although the velocity

profile shows a region of equilibrium, the flow is still developing slowly after $x/H \simeq -35$; hence the recovery of the flow is not complete with this inter-dune spacing. *Baddock et al.* [2011] reported $17.23H$ as the recovery distance of a barchan dune based on the mean velocity close to the bed. Although they examined the recovery of flow for an isolated dune, their result is close to this simulation, $14.5H$. The recovery distance of flow for transverse dunes, $x/H > 25$ [*Walker and Nickling*, 2003; *Dong et al.*, 2007], and in fluvial environments, $x/H \simeq 30-50$ [*McLean and Smith*, 1986] are much larger than the current results. *Frank and Kocurek* [1996], however, reported a much smaller distance, $x/H \simeq 8$, for the flow recovery for closely spaced transverse dunes. In general, the recovery mechanism is affected by the upper wake layer over the boundary layer; the energy transfer between these two layers may enhance internal boundary layer development. After the zero-pressure gradient zone, the flow decelerates due to the adverse pressure gradient upstream of the toe, and deviates again from an equilibrium state; the velocity profile goes above the law-of-the-wall (Figure 5) as the bed shear-stress decreases.

Development of the root-mean-square (RMS) velocity fluctuations and primary Reynolds shear stress in Case 5 is shown in Figure 6. At the beginning of the zero-pressure-gradient region, the signature of the overlying wake layer appears as an outer layer peak in the profiles of u'_{rms} and $u'v'^{+}$. The profiles further downstream ($x/H = -30.0$ and -14.0) are similar to each other, and justify our conclusion that the development of the internal boundary layer slows down after $14.5H$. Spanwise and wall-normal Reynolds stresses do not show the two peaks typical of wall-bounded flows with wake interaction [*Balachandar and Patel*, 2005], where v'^{+} and w'^{+} profiles are significantly affected throughout the depth, and the level of stresses are significantly higher than that noted

in a smooth open channel flow. Profiles at the toe of the downstream dune, after a zone of deceleration, shows a significant increase of turbulence level, consistent with many observations in the literature [*Wiggs et al.*, 1996; *Walker and Nickling*, 2002, 2003; *Parsons et al.*, 2004a; *Weaver and Wiggs*, 2011]. The sustained sediment transport that occurs in this region, despite a decrease in the bed shear-stress, is usually explained by this increase in turbulence activity.

For smaller interdune spacings, the zero-pressure-gradient zone is much shorter; it is $1.8H$ for Case 1, $6.7H$ for Case 2, $11.9H$ for Case 3, $17.2H$ for Case 4, and $35.5H$ for Case 5. Figure 7 shows the velocity profiles in wall units at the end of the zero-pressure gradient zone of the simulations, and shows the region of deceleration at the toe of the downstream dune to start earlier for larger interdune spacings. The internal boundary layer is still in significant development at a small interdune spacing, while the difference between Cases 4 and 5 is small, especially if we consider the very large difference between their interdune spacings, $24.58H$.

The effect of interdune spacing on the Reynolds stresses in the toe region of dunes is shown in Figure 8. As the interdune spacing decreases, the streamwise velocity fluctuations in the boundary layer decrease, but the wall-normal and spanwise fluctuations increase at the same time as the second peak in u'^{+} increases; the Reynolds shear stress remains unchanged close to the wall, while in the overlying layer the wake region is stronger for smaller interdune spacings. The decrease in the internal boundary layer stresses is related to a shorter development distance, and the increase in the wake layer stresses is related to a shorter decay distance of the upstream separated shear layer. If turbulence activity near the bed sustains sediment transport at the toe of the dune [*McKenna Neu-*

man et al., 2000], then sediment transport in this region should decrease with decreasing interdune spacing; this may explain the bedform repulsion effects found in deserts [*Ewing and Kocurek*, 2010] and experiments [*Endo et al.*, 2004] in which, if the approaching upstream dune is close to a downstream one (less than one dune length), it absorbs the dune by halting sediment transport in the toe region. Our results also indicate that the sediment transport at the toe may be decreased for distances of this order.

The skin friction coefficient,

$$C_f = \frac{\tau_w}{1/2\rho U_\infty^2}, \tag{4}$$

along the stoss side of dunes on the centerline symmetry plane is shown in Figure 9, where τ_w is the bed shear stress. The skin friction increases as the flow rises along the stoss side and reaches the crest at $x/H = -0.1$. The interdune spacing affects the friction coefficient at the toe, $x/H = -8.0$, which changes by about 30%, while along the stoss slope the difference between cases is small. With larger interdune spacings, the bed shear-stress is smaller, and any difference in sediment transport caused by the mean shear stress would likely not be significant. Note that the skin friction oscillates along the stoss side due to the waviness of the surface of the model; the skin friction has a minimum at $x/H = -7.6$ where the deceleration is maximum and the stoss side of the dune starts. The second minimum in the skin friction occurs at $x/H = -5.0$ due to a local deceleration of flow caused by these surface waves.

Figure 10 shows turbulence statistics along a line $0.1H$ above the bed. Through most of the zero-pressure gradient region, this line lies in the buffer layer. All cases present similar profiles; two peaks are present at the dune toe and on the stoss side. The peak at the toe, $x/H \simeq -8.0$, corresponds to flow deceleration which enhances turbulence; the second

peak at $x/H \simeq -5.0$ corresponds to the location where the wall stress has local minima (Figure 9). Reynolds stresses decay in the accelerating-flow region on the stoss side, even without the normalization of stresses with the bed-shear stress. The Reynolds shear stress (Figure 10*(d)*) is negative at the dune toe, but changes sign in the acceleration region. *Baddock et al.* [2011] observed a similar behavior and related this to the curvature of the bed, which is highest there; hence the definition of quadrants is altered and a positive value of $u'v'$ does not mean that the turbulence activity is fundamentally altered. We examined this conclusion by rotating the co-ordinate frame into parallel- and normal-to-bed co-ordinates; the rotation is a maximum at $x/H \simeq -5.0$ and is about 11^o with respect to x. The Reynolds shear stress shown for Cases 2 and 4 in Figure 11 is negative in the new system of co-ordinates; the peak at $x/H = -5.0$ disappears when the stress is not normalized with the wall-shear stress and in general $\langle u'v' \rangle / U_\infty^2$ increases slightly over the stoss side due to acceleration.

At the dune toe, where the stoss side begins, the streamwise velocity fluctuations (Figure 10*(a)*) are higher for Cases 4 and 5 (larger interdune spacing) by over 30%. The wall-normal and spanwise turbulence intensities, on the other hand, are significantly larger for small interdune spacings (Cases 1 and 2); the large differences in the intensities are consistent along the stoss side, and are not a local effect. We conjecture that penetration of the wake layer into the internal boundary layer at small interdune spacing causes a boost in the wall-normal and spanwise intensities all along the stoss side. We examined the budgets of the normal Reynolds stresses to understand the contribution of the wake layer to the turbulence intensities over the stoss side of dunes; significant differences exist between Cases 1 and 5 in $-\langle \overline{u} \rangle \partial \langle v'v' \rangle / \partial x$ and $-\langle w' \partial p' / \partial z \rangle / \rho$ that are dominant terms in

the mean-flow advection and the pressure transport of the wall-normal Reynolds stress, $\langle v'v' \rangle$, and the spanwise normal Reynolds stress, $\langle w'w' \rangle$, budgets respectively; these terms are larger in Case 1 by a factor greater than two.

At the dune toe, interdune spacings smaller than 1.02λ do not allow the wall turbulence to be amplified as the flow decelerates. Over the stoss side, the wake region overlying the internal boundary layer interacts with the wall region and enhances the wall-normal and spanwise turbulence in the cases with interdune spacings smaller than 0.68λ. Additionally, over the second half of the stoss side, the flow accelerates, which decreases the turbulence, but increases the skin friction. These modifications of the turbulence characteristics can be expected to affect significantly the sediment transport.

The flow separation at the crest produces a strong shear layer, which destabilizes the flow and increases turbulence. The Reynolds shear stress contours, shown in Figure 3, already highlight its importance. Velocity, turbulent kinetic energy, and Reynolds shear stress profiles along three vertical lines passing through the separated-shear layer are shown in Figure 12. $\langle v'v' \rangle / U_\infty^2$ and $\langle u'v' \rangle / U_\infty^2$ are significant in the shear layer where the mean flow bends towards the bed; $\langle w'w' \rangle / U_\infty^2$ presents significant turbulence in the shear layer and near the bed around the reattachment point. Profiles at $x/H = 2.0$, inside the separation bubble, show the reversed flow near the bed and the shear layer above it. The mean velocity in the separation bubble does not change significantly with interdune spacing, but the downward flow in the separated-shear layer is faster for more closely-spaced cases; the maximum vertical velocity for Case 5 is only 56% of the that in Case 1. Turbulent kinetic energy and the Reynolds shear stress are smaller for largely-spaced dunes (Case 5) since the separated flow has a smaller velocity gradient, $\partial \langle \overline{u} \rangle / \partial y$ (Figure

452 12*(a)*). The difference in the turbulent kinetic energy (Figure 12*(c)*) and the Reynolds
453 shear stress (Figure 12*(d)*) decreases as the profiles move downstream and the effect of
454 the interdune spacing becomes negligible. On the other hand, vertical velocities (Figure
455 12*(b)*) coincide with each other at $x/H = 10.0$ except for Case 1, where the profile is at
456 the toe of the following dune, and the vertical velocity is directed upwards. In conclusion,
457 large-moderate interdune spacings do not affect the turbulence statistics of the separated-
458 shear layer significantly, and by $10H$ after the crest all statistics converge. However, if
459 the spacing between the dunes is small, here less than 0.34λ, this conclusion is invalid as
460 the flow can develop for less than $10H$ before the next dune is reached.

3.2. Mean-flow three-dimensionality

461 In Figure 13 we show mean streamlines near the bed (realeased at $y/H = 0.1$ upstream
462 of the dune). The streamlines close to the centerline plane (labeled by number 1) diverge
463 as they rise on the stoss side, separate at the crest, then move towards the bed. Away from
464 the centerline plane, the streamlines (labeled by number 2, Figure 13) diverge toward the
465 horns and separate at the crest, but, once they enter the separation bubble, they meander
466 towards the horns while remaining near the bed. Streamlines far away from the centerline
467 plane (labeled by number 3, Figure 13) diverge toward the horns and never separate.
468 Contours of the velocity magnitude show that streamlines on the bed are accelerated
469 after passing the barchan.

470 The bed shear-stress is strong over the stoss side of dunes close to the crest (Figure
471 14). At the dune toe, the flow diverges from the centerline plane, and the bed stress
472 decreases, as shown in the profile of Figure 9; away from the centerline and along the
473 horns the stress is large, as the flow rises up the stoss side. Figure 14 shows that the

separation bubble does not extend all the way along the horns: the separated flow at the crest reattaches on the bed and, due to the three-dimensionality of the separation line, a nodal point of attachment appears away from the symmetry plane (point $p2$, blue bullet in Figure 14). The bed shear-stress is larger downstream of this point: high-momentum fluid that separated at the crest reattaches, increasing the pressure and the stress. Compared to the streamlines around the nodal point of attachment, a saddle point of separation appears downstream of the dune on the symmetry plane (point $p1$, red bullet in Figure 14) where the shear stress is small and the near-bed flow converges towards the centerline plane from the sides. The separation bubble contains a large secondary flow, and a few small secondary flow regions, over the lee side of the dune, which cause weak points of separation and attachment. These features close to the bed are often observed in the separation bubble of three-dimensional objects [*Chapman and Yates*, 1991; *Omidyeganeh and Piomelli*, 2013]. All other cases in our simulations present a similar trend; of note, the bed shear-stress does not change significantly with dune spacing (Figure 9 and 16*(a)*). From a series of streamlines over the stoss side of the dune, we note that the separation bubble and the reattached flow converge to a single streamline along the horn and leave the dune from that side, consistent with Figure 13. The observation that barchan dunes lose sediment from the horns [*Hersen et al.*, 2004; *Franklin and Charru*, 2011], is explained by our results.

The dune creates two streamwise vortices that induce secondary flow. In Figure 15 contours of mean streamwise vorticity and streamlines in the cross planes (i.e., calculated from V and W components of the velocity only) are shown. As the flow near the bed approaches the dune it diverges toward the closest horn. This induces convergence of

high-momentum fluid away from the bed towards the centerline plane, which results in formation of two counter-rotating streamwise vortices aligned with each horn, and with a diameter close to the flow depth. The strength of these vortices is two orders of magnitude smaller than the vorticity of the secondary flow within the separation bubble. This pattern of secondary flow is consistent for all other cases, but the vorticity magnitude decreases as the interdune spacing increases. This may be due to the periodic boundary conditions, since each vortex is amplified by the next dune in the array. Note that in the experiments of *Palmer et al.* [2012] either a single dune or two dunes only were considered. The streamwise vortices were, therefore, weaker than in the present case, in which an infinite array of barchans is considered, each dune strengthening the vortices generated upstream. Since the downwash in the plane of symmetry is weaker, lower streamwise velocity should be expected in this plane, compared to the simulations, which was observed in Figure 4*(a-c)*.

We have already observed how the interdune spacing affects turbulent statistics. In Figure 16, we show the vertical (wall-normal) and spanwise Reynolds stresses along a line $0.1H$ from the bed, in the middle of the stoss side ($x/H \simeq -5.0$). The bed shear-stress is not affected significantly by the interdune spacing (Figure 16*(a)*) and over the stoss side of the dune, $-4.0 \leq z/H \leq 4.0$, the Reynolds stress is smaller due to the divergence of flow from the centerline plane, shown in Figure 14. $\langle v'v' \rangle / U_\infty^2$ drops over the stoss side while along the horns it increases significantly; at small interdune spacing (Case 1), due to the sheltering effect of the upstream dune, the down flow of the fluid is more significant, which carries turbulence structures to the near-wall region. The spanwise normal Reynolds stress (Figure 16*(c)*) has a peak on the centerline of the dune and is larger for smaller interdune

spacings. In Case 5, when the distance between dunes is large, $\langle w'w' \rangle / U_\infty^2$ is uniform across the channel, indicating that the sheltering effect of the upstream dune has become much weaker. The effect of the stronger turbulent motions on the sediment transport, and of the turbulence structures penetrating into the internal boundary layer, deserve further future study.

Budgets of turbulent kinetic energy on the stoss side are shown in Figure 17 for Cases 1 and 5. The dune-to-dune interaction, which is strong in Case 1, results in a much thicker layer in which the turbulent kinetic energy transport is important. Two factors contribute to this effect: the shear layer produced by the upstream dune, which overlays the near-bed boundary layer, and the motion induced by the streamwise vortices, which is much stronger in Case 1. The contribution of the shear layer is most significant in the production of TKE and pressure transport, while the footprint of the streamwise vortices is very clear in the dissipation contours. The mean secondary flow also advects wall turbulence away from the dune (Figure 17*(c,d)*); in Case 1, mean flow advection is also significant in the wake region (Figure 17*(d)*).

3.3. Instantaneous flow structures

Contours of u' on a plane parallel to the bed and close to it are shown in Figure 18 for the cases with the largest and smallest interdune spacings, Cases 5 and 1. The flow approaching the dune in Case 5 has the streaky structure characteristics of a smooth open channel, with alternating streaks of low- and high-momentum fluid. Note the predominance of low-speed streaks in the region immediately inboard of the horns, due to the up flow of the streamwise vortices. Flow acceleration over the stoss side of the dune tends to elongate the streaks, consistent with the observations of *Franklin and Charru* [2011],

who observed streamwise stripes with regular spacing on the stoss side of their barchan dune. On the lee side, spanwise-oriented structures are observed between the horns in the recirculation region. Downstream of reattachment the structures are reorganized and within a dune length, the low- and high-speed streaks are reformed. Case 1 presents different characteristics; the streaks are shorter and the footprint of the overlying streamwise vortices is stronger. The magnitude of fluctuations is larger for Case 1; the closely-spaced dune arrangement enhances the wall turbulence, and would also affect sediment transport in mobile-bed barchans.

Isosurfaces of the second invariant of the velocity-gradient tensor Q,

$$Q = -\frac{1}{2}\frac{\partial \overline{u_i}}{\partial x_j}\frac{\partial \overline{u_j}}{\partial x_i} \tag{5}$$

and pressure fluctuations p' are shown for Cases 5 and 1, respectively, in Figures 19 and 20. Q has been shown to be very effective in visualizing small turbulent eddies, while p' is better at highlighting the larger coherent structures [*Dubief and Delcayre*, 2000]. The white circles highlight some turbulent structures. Narrow elongated streamwise structures are observed over the stoss side of the dune (region 1 in Figure 19*(a)*); these structures are longer than the typical wall streaks, as observed before, because of the acceleration of the flow on the windward slope. Separated spanwise vortices at the crest are identified by both Q and p' (region 2). These rollers are generated by a Kelvin-Helmholtz instability of the strong shear layer after separation of flow at the crest and, while convected downstream, undergo a three-dimensional instability and lose their coherence (region 3); downstream of the dune, signs of turbulent activity from the wake region of the upstream dune are still observed. Away from the centerline plane, large coherent structures are rarely observed (those in region 4 are an example); when they occur, they do so in the outer region of

565 the flow. These structures are convected downstream and away from the centerline plane
566 by the mean secondary flow (Figure 15). Pressure fluctuations identify large but weak
567 structures away from the bed (region 5) that are not observed by the Q criterion. Coherent
568 structures away from the bed most frequently occur outboard of the horns (regions 4 and
569 5), where the up flow of the secondary flow enhances their advection towards the free-
570 surface.

571 For closely spaced dunes (Case 1) the eddies are significantly more coherent (Figure
572 20). Note that the isosurface levels of p' in this Figure are twice as large as those shown
573 in Figure 19. Most of the structures are observed close to the centerline symmetry plane
574 (regions 1 and 2); outside the horns, large scale packets of eddies rarely appear (region
575 3 is an example). Isosurfaces of p' identify the rollers at the crest of dunes (ellipsoid 1
576 in Figure 20*(b)*), which are bigger, wider and more coherent in Case 1 compared to Case
577 5, due to a larger velocity gradient in the separated-shear layer (Figure 4). For closely-
578 spaced dunes, the coherent structures convected downstream contribute to flow over the
579 stoss side (region 2), and alter the structures close to the bed (Figure 18).

580 The contours of spanwise vorticity fluctuations and streamwise velocity fluctuations
581 (Figure 21) also show the significant influence of interdune spacing on the flow structures.
582 In Case 1, the flow is affected by the bed roughness much further from the bed, up to $5H$,
583 while in Case 5 very few structures are observed above $2H$. In the separated shear layer,
584 small-scale vortices are observed for both cases, but downstream the eddies are confined
585 to the wake region in Case 5, while the separated eddies mix with the upper part of the
586 shear layer in Case 1. The mean turbulent kinetic energy and Reynolds shear stress are
587 more than 20% larger in the separated shear layer of Case 1 than Case 5 (Figure 12*(c,d)*).

Coherent structures approaching the stoss side of the dune in Case 5 are elongated in the streamwise direction, typical of a boundary layer (Figure 21*(a)*), while in closely-spaced dunes they more resemble a wake structure, with similar scales in streamwise and normal directions (Figure 21*(b)*). The contribution of these structures to the turbulent kinetic energy is significant, as shown by *Palmer et al.* [2012].

4. Discussion and conclusions

The flow over barchan dunes has been studied through a series of numerical simulations of an infinite array of dunes, with variable spacing between dunes in the streamwise direction. The flow has some characteristics in common with that over transverse dunes (deceleration and acceleration of flow over the stoss side, flow separation and formation of a shear layer at the crest, reattachment on the bed and development of an internal boundary layer), but the complex three-dimensional shape of barchans introduces mean secondary flow across the channel and alters turbulence over the stoss side. The current simulations are validated against experiments [*Palmer et al.*, 2012] and provide a comprehensive three-dimensional picture of mean flow characteristics and instantaneous flow structures.

Barchan dunes induce the formation of two counter-rotating streamwise vortices along each horn. These vortices direct high-momentum fluid toward the symmetry plane and low-momentum fluid near the bed away from the centerline. In our configuration with barchans aligned in the spanwise direction, and with the periodic boundary condition used, the streamwise vortices become stable.

The flow near the bed, upstream of the dune, diverges from the centerline plane, decelerates and rises on the stoss side of the dune. Flow close to the centerline plane separates at the crest and reattaches, while far from the centerline plane and along the horns flow

separation occurs intermittently. The flow in the separation bubble meanders towards the horns and leaves the dune. We note that the flow in the separation bubble may be capable of transporting high concentrations of sediment that will exit the dune from the horns, which explains many observations in field and laboratory measurements indicating that barchans loose sediment downstream via their horns.

The characteristics of the separated-shear layer are altered by the interdune spacing; the separation bubble is smaller, the separated-shear layer is stronger, and the bed shear-stress is larger at smaller interdune spacing. The statistics of the shear layer converge at a distance downstream, $x/H = 10.0$, except for Case 1, in which the shear layer responds more strongly to the presence of the downstream dune. The separated flow at the crest reattaches on the bed, except on the symmetry plane, where a weak saddle point of separation appears on the bed. The features of the separation bubble are similar to other three-dimensional dunes; a nodal point of reattachment appears outside the centerline plane where high-momentum fluid reattaches, and the bed shear-stress is larger downstream of this point than at the center of the dune.

An internal boundary layer develops downstream of the reattachment region under zero-pressure gradient, for a distance of $35.5H$ in Case 5; the velocity profiles approach the logarithmic law-of-the wall from below and present a small range of logarithmic behavior. The recovery process of the internal boundary layer slows down after approximately $14.5H$, and then the flow decelerates as it approaches the stoss of the downstream dune. The development of the internal boundary layer has the same features in all cases, but the length of the zero-pressure gradient region decreases to $1.8H$ for Case 1; the internal boundary layer is at the beginning of its development at this distance and the mixing

of the overlying wake layer with the boundary layer is still significant. At the toe, the streamwise normal Reynolds stress, likely responsible for sustained sediment transport of the retarded flow, decreases at small interdune spacings.

Over the stoss side of the dune, the skin friction increases towards the crest, and also increases slightly at smaller interdune spacing. The acceleration of the flow on the stoss side decreases the Reynolds stresses as the flow rises up the dune, but the spanwise and wall-normal Reynolds stresses are significantly higher along the stoss side for Cases 1 and 2 (with small interdune spacing) due to the sheltering effect of the overlying wake region advected from the upstream dune. The largest interdune spacing (2.38λ, where λ is the length of the barchan model) presents characteristics similar to those of an isolated dune in the experiment, indicating that at this distance the sheltering effect of the upstream dune is very weak although the mean velocity is not logarithmic yet. Turbulent kinetic energy budgets show the significance of the production and dissipation of turbulence in the separated-shear layer and in the attached shear layer on the bed; over the stoss side, pressure transports energy from the overlying wake layer towards the bed, and contributes more to the energy transport at smaller interdune spacings.

The interdune spacing significantly alters the turbulent flow over the stoss side of the downstream dunes; coherent high- and low-speed streaks are shorter but stronger, and the spanwise normal Reynolds stress is larger at smaller interdune spacing, where spanwise-oriented structures are observed near the bed; they carry the signatures of the separated vortices at the crest of the upstream dune. To the sides of the barchans, typical wall turbulence structures are observed, but coherent eddies generated in the separated-shear layer due to Kelvin-Helmholtz instability are dominant. Coherent structures are gener-

ated more frequently with smaller interdune spacings; they are advected further from the bed and remain between the horns, while at larger interdune spacing the structures are advected in the spanwise direction with the mean streamwise vortices and reach the outside of the dunes.

These results show the complexities introduced to the flow field by dune three-dimensionality and the significant influence of dune spacing at close bedform separations. They also illustrate that models of flow proposed for isolated bedforms require modification where the flow fields of dunes interact, and that these interactions will modify the intensity and structure of turbulence generated that will then influence the stoss side of the downstream dune. This modulation of dune flow fields will likely be significant in influencing sediment transport and the nature of dune migration [*Endo et al.*, 2004], and suggests that future work should examine these interactions more fully and in cases where the bed is fully mobile.

Acknowledgments. This research was supported by the Natural Sciences and Engineering Research Council (NSERC) under the Discovery Grant program. The authors thank the High Performance Computing Virtual Laboratory (HPCVL), Queen's University site, for computational support. MO acknowledges the partial support of NSERC under the Alexander Graham Bell Canada NSERC Scholarship Program. UP also acknowledges the support of the Canada Research Chairs Program.

References

Allen, J. (1968), *Current ripples: their relation to patterns of water and sediment motion*, North-Holland Pub. Co.

677 Andreotti, B., P. Claudin, and S. Douady (2002), Selection of dune shapes and ve-
678 locities part 1: Dynamics of sand, wind and barchans, *Euro. Phys. J. B*, *28*, doi:
679 10.1140/epjb/e2002-00236-4.

680 Armenio, V., and U. Piomelli (2000), A Lagrangian Mixed Subgrid-Scale Model in Gen-
681 eralized Coordinates, *Flow, Turb. Combust.*, *65*, 51–81.

682 Baddock, M. C., I. Livingstone, and G. F. S. Wiggs (2007), The geomorphological signif-
683 icance of airflow patterns in transverse dune interdunes, *Geomorphology*, *87*, 322–336.

684 Baddock, M. C., G. F. S. Wiggs, and I. Livingstone (2011), A field study of mean and
685 turbulent flow characteristics upwind, over and downwind of barchan dunes, *Earth Surf.*
686 *Proc. Landf.*, *36*, 1435–1448, doi:10.1002/esp.2161.

687 Bagnold, R. A. (1941), *The Physics of Blown Sand and Desert Dunes*, Methuen, London.

688 Balachandar, R., and V. C. Patel (2005), Velocity measurements in a developed open
689 channel flow in the presence of an upstream perturbation, *J. Hydr. Res.*, *43*(3), 258–
690 266.

691 Best, J. L. (2005), The fluid dynamics of river dunes: A review and some future research
692 directions, *J. Geophys. Res.*, *119*(F04S02), 1–21.

693 Breed, C. S., M. J. Grolier, and J. F. McCauley (1979), Morphology and distribution
694 of common 'sand' dunes on mars: Comparison with the earth, *J. Geophys. Res.*, *84*,
695 8183–8204.

696 Chapman, G. T., and L. A. Yates (1991), Topology of flow separation on three-dimensional
697 bodies, *Appl. Mech. Rev.*, *44*(7), 329–345.

698 Charru, F., and E. M. Franklin (2012), Subaqueous barchan dunes in turbulent shear
699 flow. part 2. fluid flow, *J. Fluid Mech.*, *694*, 131–154.

Choi, H., and P. Moin (2012), Grid-point requirements for large eddy simulation: Chapman's estimates revisited, *Phys. Fluids*, *011702*, 011,702–1—5.

Dong, Z., G. Qian, W. Luo, and H. Wang (2007), Simulation of the effects of stoss slope on the lee airflow pattern over a two-dimensional transverse dune, *J. Geophys. Res.*, *112*(F03019), doi:10.10292006JF000686.

Dubief, Y., and F. Delcayre (2000), On coherent vortex identification in turbulence, *J. Turbul.*, *1*, 1–22.

Endo, N., K. Taniguchi, and A. Katsuki (2004), Observation of the whole process of interaction between barchans by flume experiments, *Geophys. Res. Lett.*, *31*, L12,503, doi:10.1029/2004GL020168.

Ewing, R. C., and G. Kocurek (2010), Aeolian dune interactions and dune-field pattern formation: White sands dune field, new mexico, *Sedimentology*, *57*, 1199–1219.

Fernandez, R., J. Best, and F. Lopez (2006), Mean flow, turbulence structure and bedform superimposition across the ripple-dune transition, *Wat. Resources Res.*, *42*(W05406), doi:10.1029/2005WR004330.

Finkel, H. J. (1959), The barchans of southern peru, *J. Geology*, *67*, 614–647.

Frank, A., and G. Kocurek (1996), Toward a model for airflow on the lee side of aeolian dunes, *Sedimentology*, *43*, 451–458.

Franklin, E. M., and F. Charru (2011), Subaqueous barchan dunes in turbulent shear flow. part 1. dune motion, *J. Fluid Mech.*, *675*, 199–222.

Germano, M., U. Piomelli, P. Moin, and W. H. Cabot (1991), A dynamic subgrid-scale eddy viscosity model, *Phys. Fluids A*, *3*, 1760–1765.

722 Hardisty, J., and R. J. S. Whitehouse (1988), Effect of bedslope on desert sand transport,
723 *Nature*, *334*, 302.
724 Hermann, H. J., J. S. Andrade Jr., V. Schatz, G. Sauermann, and E. J. R. Parteli (2005),
725 Calculation of the separation streamlines of barchans and transverse dunes, *Physica A*,
726 *357*, 44–49, doi:10.1016/j.physa.2005.05.057.
727 Hersen, P., K. H. Andersen, H. Elbelrhiti, B. Andreotti, P. Claudin, and S. Douady (2004),
728 Corridors of barchan dunes: Stability and size selection, *Phys. Rev. E*, *69*(011304), 1–12.
729 Hesp, P. A., and K. Hastings (1998), Width, height and slope relationships and aerody-
730 namic maintenance of barchans, *Geomorphology*, *22*, 193–204.
731 Hirt, C. W., and B. D. Nicholas (1981), Volume of fluid (vof) method for the dynamics
732 of free boundaries, *J. Comput. Phys.*, *39*, 201–225.
733 Iversen, J. D., and K. R. Rasmussen (1994), The effect of surface slope on saltation
734 threshold, *Sedimentology*, *41*, 721–728.
735 Jackson, P. S., and J. C. R. Hunt (1975), Turbulent wind flow over a low hill, *Quarterly*
736 *J. Royal Meteo. Soc.*, *101*, 929–955.
737 Jordan, S. A. (1999), A large-eddy simulation methodology in generalized curvilinear
738 coordinates, *J. Comput. Phys.*, *148*(2), 322–340.
739 Kim, J., and P. Moin (1985), Application of a fractional step method to incompressible
740 Navier-Stokes equations, *J. Comput. Phys.*, *59*, 308–323.
741 Kocurek, G., R. C. Ewing, and D. Mohrig (2010), How do bedform patterns arise? new
742 views on the role of bedform interactions within a set of boundary conditions, *Earth*
743 *Surf. Proc. Landf.*, *35*, 51–63, doi:10.1002/esp.1913.

Kroy, K., S. Fischer, and B. Obermayer (2005), The shape of barchan dunes, *J. Phys. Condens. Matter*, *17*, S1229–S1235.

Lancaster, N. (1985), Variations in wind velocity and sand transport rates on the windward flanks of desert sand dunes, *Sedimentology*, *32*, 581–593.

Lancaster, N. (1995), *Geomorphology of desert dunes*, Routledge, New York.

Lancaster, N., W. G. Nickling, C. McKenna Neuman, and V. E. Wyatt (1996), Sediment flux and airflow on the stoss slope of a barchan dune, *Geomorphology*, *17*, 55–62.

Leonard, A. (1974), Energy cascade in large-eddy simulations of turbulent fluid flows, *Adv. Geophys.*, *18A*, 237–248.

Lettau, K., and H. H. Lettau (1969), Bulk transport of sand by the barchans of la pampa la hoja in southern peru, *Zeitschrift fūr Geomorphologie*, *13*, 182–195.

Lima, A. R., G. Sauermann, H. J. Herrmann, and K. Kroy (2002), Modelling a dune field, *Physica A*, *310*, 487–500.

Livingstone, I., G. F. S. Wiggs, and C. M. Weaver (2007), Geomorphology of desert sand dunes: A review of recent progress, *Earth Sci. Rev.*, *80*, 239–257.

McCullogh, D. S., and R. J. Janda (1964), Subaqueous river channel barchan dunes, *J. Sed. Petrol.*, *34*, 694.

McKenna Neuman, C., N. Lancaster, and W. G. Nickling (2000), The effect of unsteady winds on sediment transport on the stoss slope of a transverse dune, silver peak, nv, usa, *Sedimentology*, *47*, 211–226.

McLean, S. R., and J. D. Smith (1986), A model for flow over two-dimensional bed forms, *J. Hydr. Engng*, *112*(4), 300–317.

766 Meneveau, C., T. S. Lund, and W. H. Cabot (1996), A Lagrangian dynamic subgrid-scale
767 model of turbulence, *J. Fluid Mech.*, *319*, 353–385.
768 Omidyeganeh, M., and U. Piomelli (2011), Large-eddy simulation of two-dimensional
769 dunes in a steady, unidirectional flow, *J. Turbul.*, *12*(42), 1–31.
770 Omidyeganeh, M., and U. Piomelli (2013), Large-eddy simulation of three-dimensional
771 dunes in a steady, unidirectional flow. part 1: Turbulence statistics, *J. Fluid Mech.*,
772 *721*, 454–483.
773 Palmer, J. A., R. Mejia-Alvarez, J. L. Best, and K. T. Christensen (2012), Particle-image
774 velocimetry measurements of flow over interacting barchan dunes, *Exp. Fluids*, *52*, 809–
775 829.
776 Parsons, D. R., G. F. S. Wiggs, I. J. Walker, R. I. Ferguson, and B. G. Garvey (2004a),
777 Numerical modelling of airflow over an idealised transverse dune, *Env. Mod. Soft.*, *19*,
778 153–162, doi:10.1016/S1364-8152(03)00117-8.
779 Parsons, D. R., I. J. Walker, and G. F. S. Wiggs (2004b), Numerical modelling of flow
780 structures over idealized transverse aeolian dunes of varying geometry, *Geomorphology*,
781 *59*, 149–164.
782 Radhakrishnan, S., U. Piomelli, A. Keating, and A. Silva Lopes (2006), Reynolds-averaged
783 and large-eddy simulations of turbulent non-equilibrium flows, *J. Turbul.*, *7*(63), 1–30.
784 Radhakrishnan, S., U. Piomelli, and A. Keating (2008), Wall-modeled large-eddy simula-
785 tions of flows with curvature and mild separation, *ASME J. Fluids Eng.*, *130*(101203).
786 Rhie, C. M., and W. L. Chow (1983), Numerical study of the turbulent flow past an airfoil
787 with trailing edge separation, *AIAA J.*, *21*, 1525–1532.
788 Schlichting, H. (1955), *Boundary-Layer Theory*, Pergamon Press, New York.

Silva Lopes, A., and J. M. L. M. Palma (2002), Simulations of isotropic turbulence using a non-orthogonal grid system, *J. Comput. Phys.*, *175*(2), 713–738.

Silva Lopes, A., U. Piomelli, and J. M. L. M. Palma (2006), Large-eddy simulation of the flow in an S-duct, *J. Turbul.*, *7*(11), 1–24.

Takahashi, S., M. Du, P. Wu, T. Maki, and S. Kawashima (1998), Three dimensional numerical simulation of the flow over complex terrain with windbreak hedge, *Env. Mod. Soft.*, *13*, 257–265.

Walker, I. J., and W. G. Nickling (2002), Dynamics of secondary airflow and sediment transport over and in the lee of transverse dunes, *Prog. Phys. Geog.*, *26*(1), 47–75.

Walker, I. J., and W. G. Nickling (2003), Simulation and measurement of surface shear stress over isolated and closely spaced transverse dunes in a wind tunnel, *Earth Surf. Proc. Landf.*, *28*, 1111–1124.

Walmsley, J. L., and A. D. Howard (1985), Application of a boundary-layer model to flow over an aeolian dune, *J. Geophys. Res.*, *90*, 10,631–10,640.

Weaver, C. M., and G. F. S. Wiggs (2011), Field measurements of mean and turbulent airflow over a barchan sand dune, *Geomorphology*, *128*, 32–41.

Wiggs, G. F. S., I. Livingstone, and A. Warren (1996), The role of streamline curvature in sand dune dynamics: evidence from field and wind tunnel measurements, *Geomorphology*, *17*, 29–46.

Wippermann, F. K., and G. Gross (1986), The wind-induced shaping and migration of an isolated dune: a numerical experiment, *Bound.-Lay. Meteorol.*, *36*, 319–334.

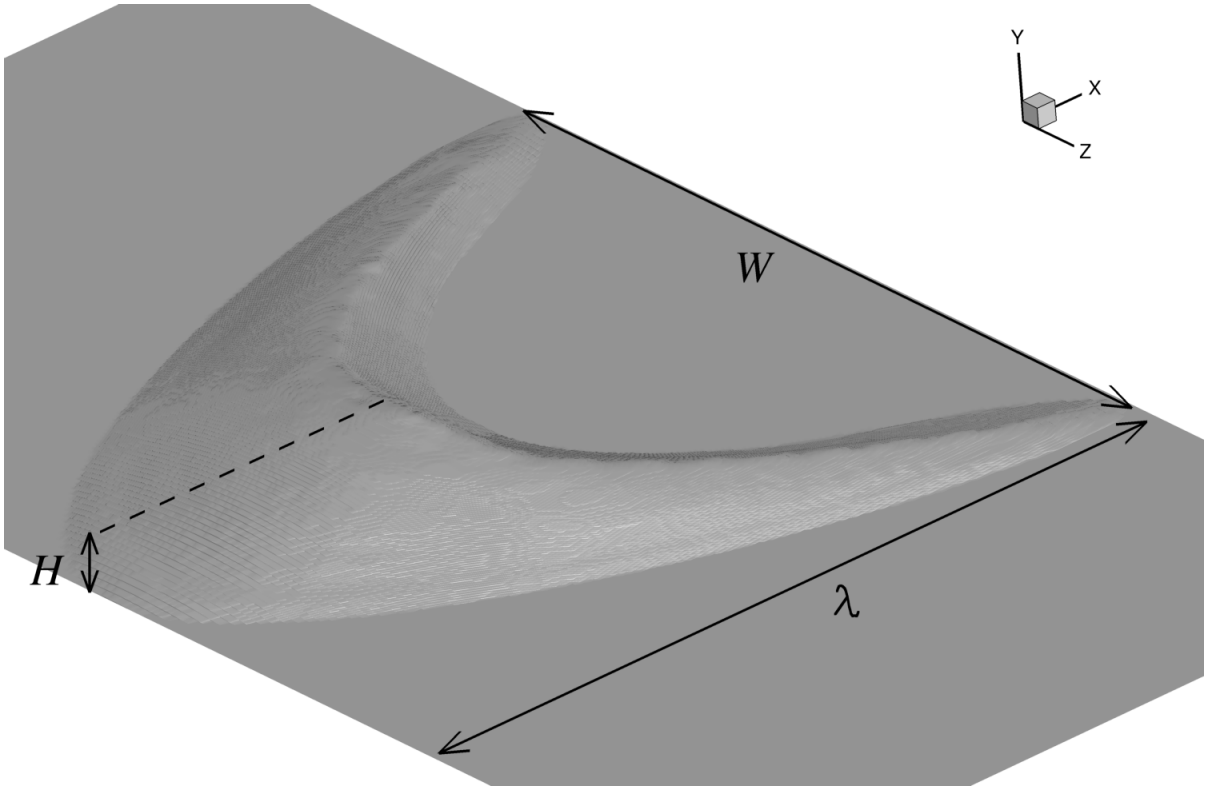

Figure 1. Geometry of the barchan dune model.

Case No.	Spacing	$N_x \times N_y \times N_z$	Δx^+_{max}	Δy^+_{max}	Δz^+_{max}
1	0.00 λ	$160 \times 281 \times 512$	28.86	0.83	10.55
2	0.34 λ	$192 \times 281 \times 512$	29.49	0.85	10.78
3	0.68 λ	$224 \times 281 \times 512$	28.67	0.82	10.48
4	1.02 λ	$256 \times 281 \times 512$	28.81	0.83	10.53
5	2.38 λ	$384 \times 281 \times 512$	27.15	0.78	9.92

Table 1. Properties of the test cases. The interdune spacing is defined as the distance between the streamwise location of the horns of upstream dune and the base of the upstream stoss side of the downstream dune.

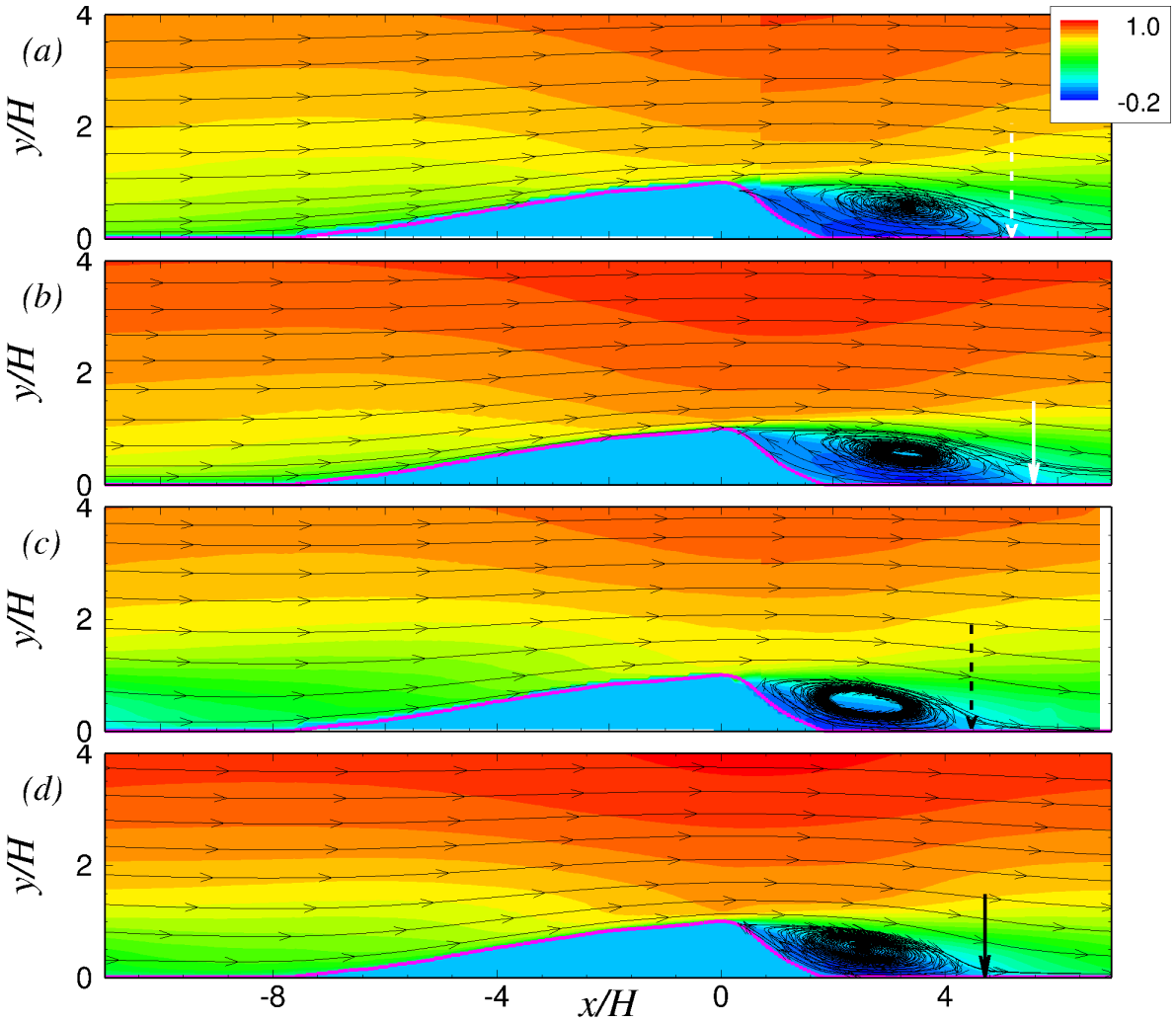

Figure 2. Contours of streamwise velocity, $\langle\overline{u}\rangle/U_\infty$, and streamlines on the centerline plane of *(a)* isolated dune [*Palmer et al.*, 2012], *(b)* Case 5, *(c)* downstream dune of zero interdune-spacing array [*Palmer et al.*, 2012], and *(d)* Case 1. Arrows show the streamwise position of the reattachment point.

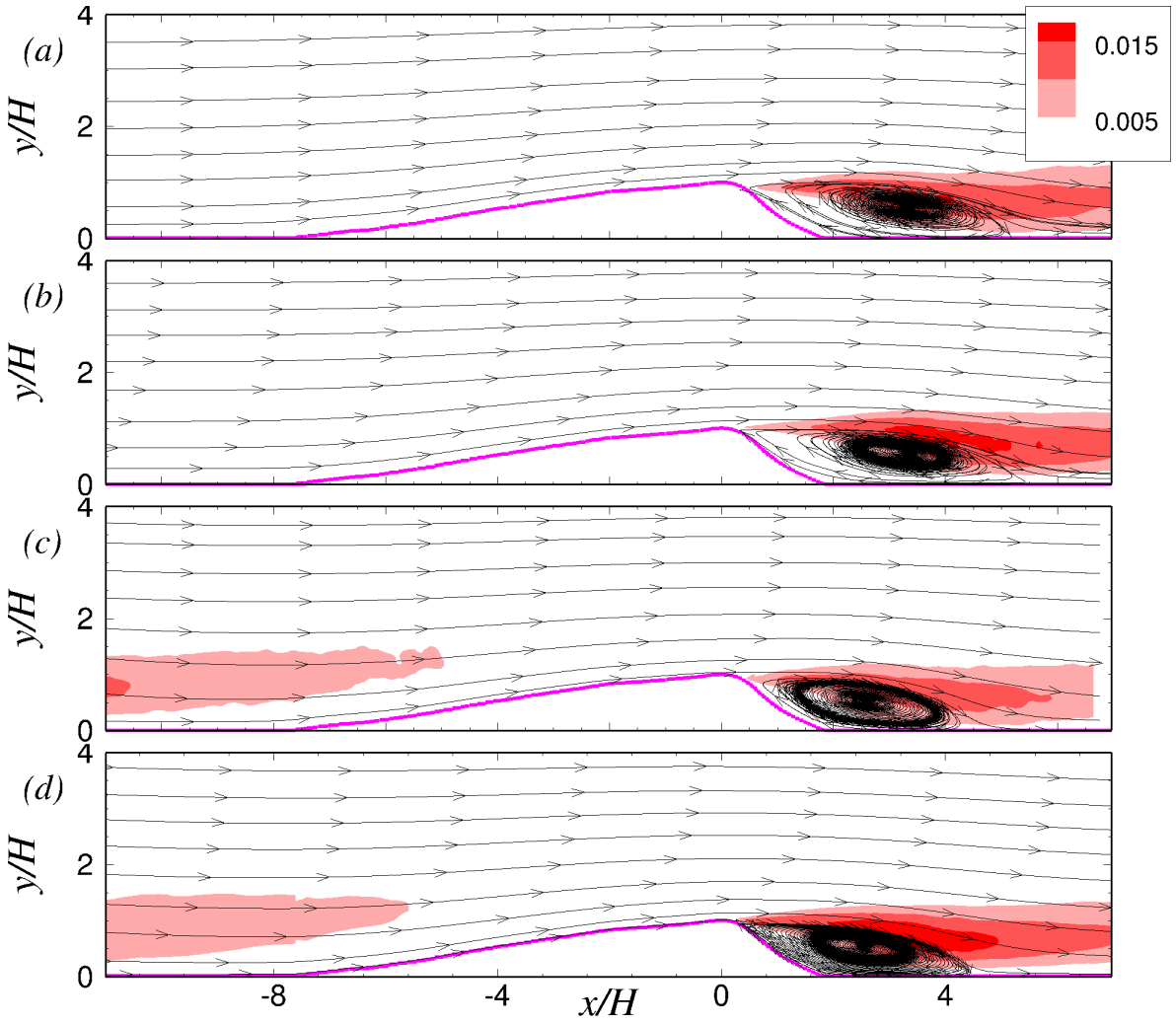

Figure 3. Contours of Reynolds shear stress, $-\langle u'v' \rangle / U_\infty^2$, and streamlines on the centerline plane of *(a)* isolated dune [*Palmer et al.*, 2012], *(b)* Case 5, *(c)* downstream dune of zero interdune-spacing array [*Palmer et al.*, 2012], and *(d)* Case 1.

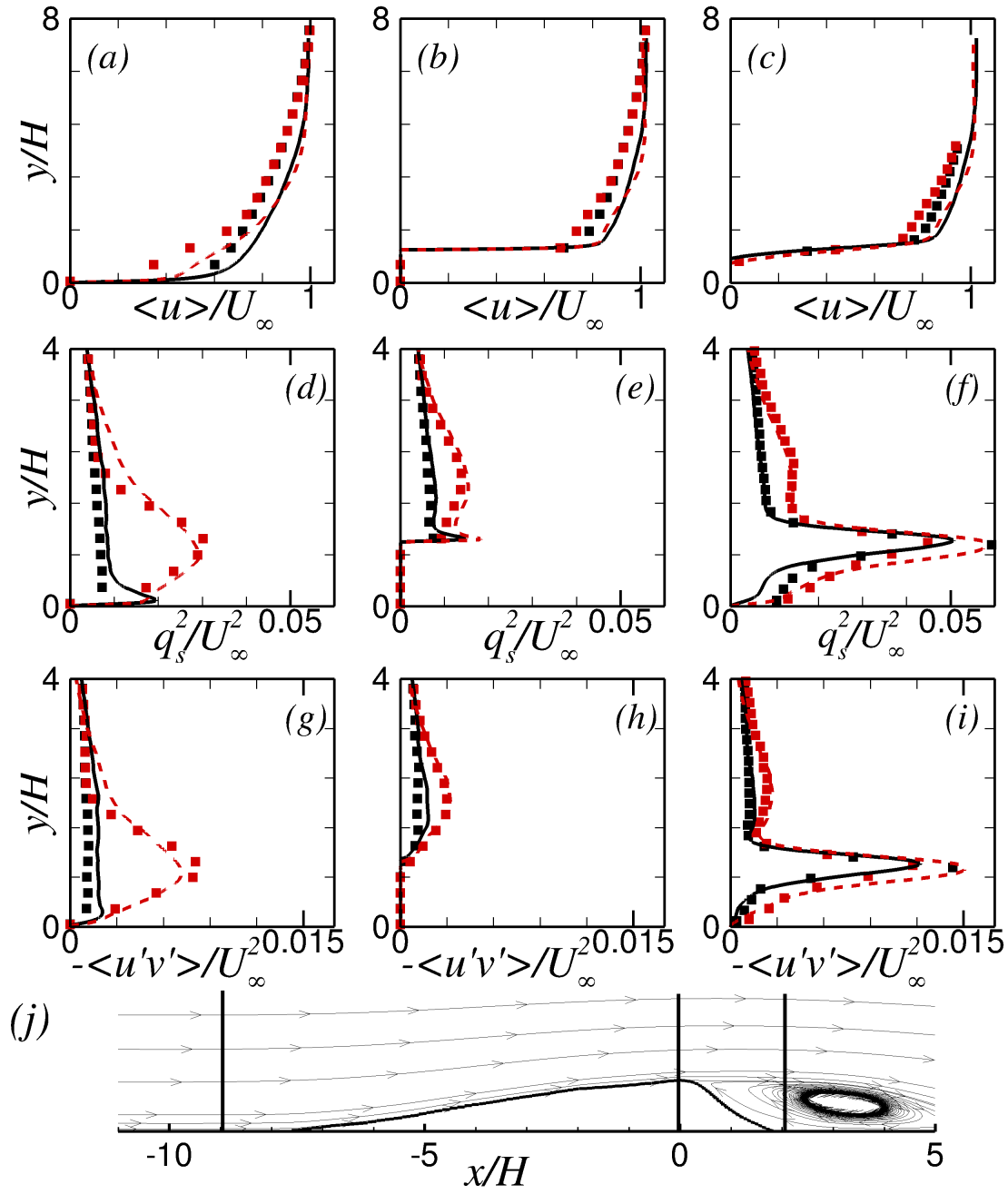

Figure 4. *(a-c)* Streamwise velocity profiles, *(d-f)* Planar turbulent kinetic energy, and *(g-i)* Reynolds shear stress at *(a,d,g)* $x/H = -9.0$, *(b,e,h)* $x/H = 0.0$, and *(c,f,i)* $x/H = 2.0$; —— Case 5, - - - Case 1, ■ isolated dune, and ■ zero spacing in the experiment [*Palmer et al.*, 2012].

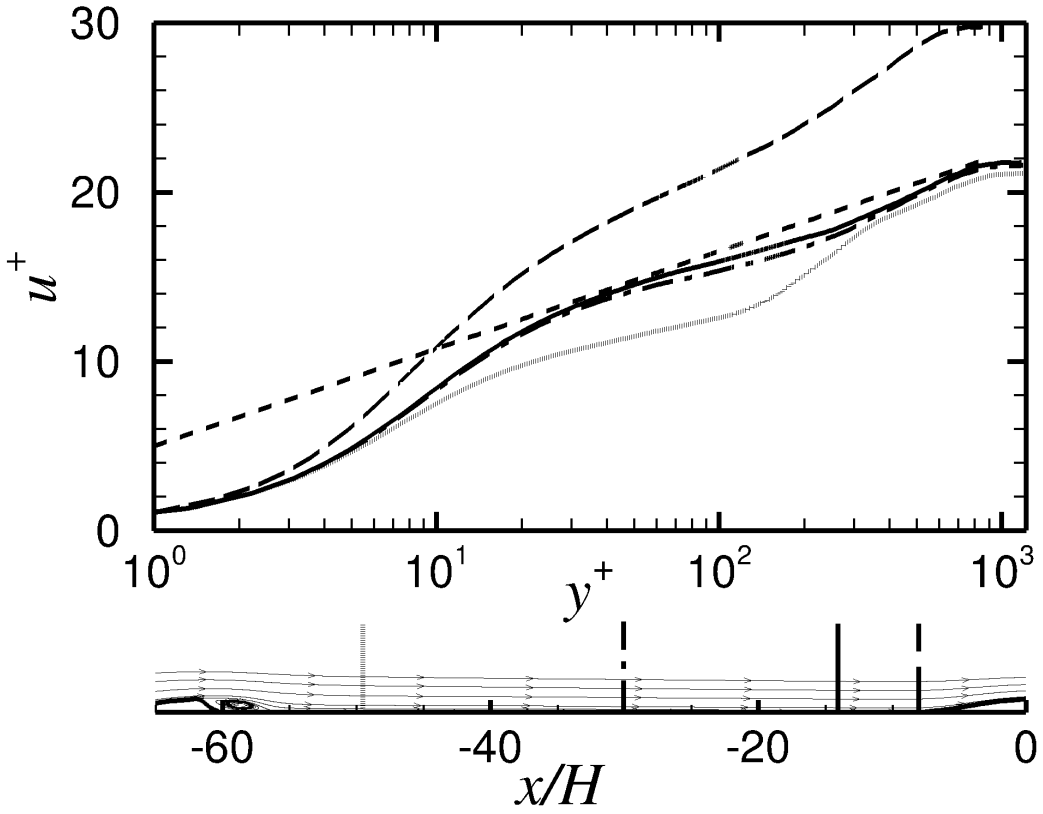

Figure 5. Mean velocity profiles in wall units for Case 5 at the locations shown in *(d)*.

--- Logarithmic law-of-the-wall: $u^+ = \ln y^+/\kappa + 5.0$.

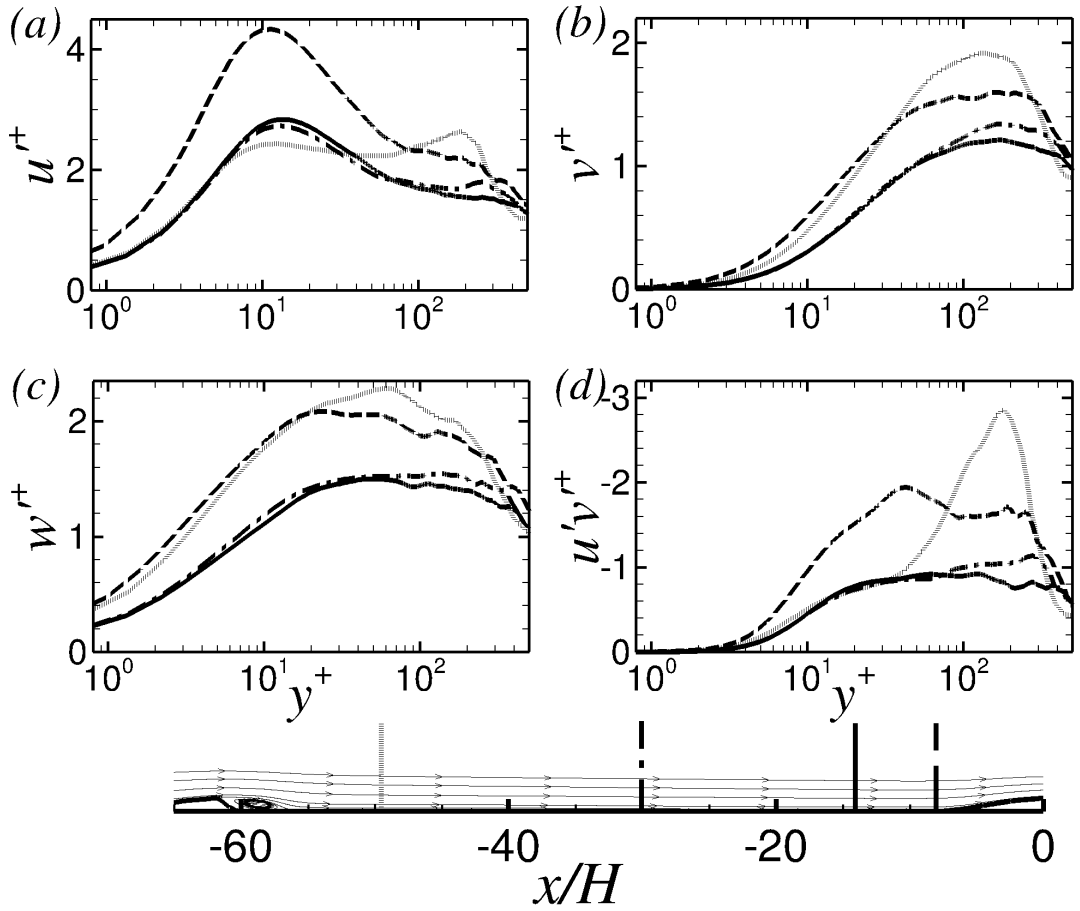

Figure 6. RMS velocity profiles and Reynolds shear stress in wall units for Case 5 at the locations shown in *(d)*; *(a)* u'_{rms}, *(b)* v'_{rms}, *(c)* w'_{rms}, *(d)* $u'v'^{+}$.

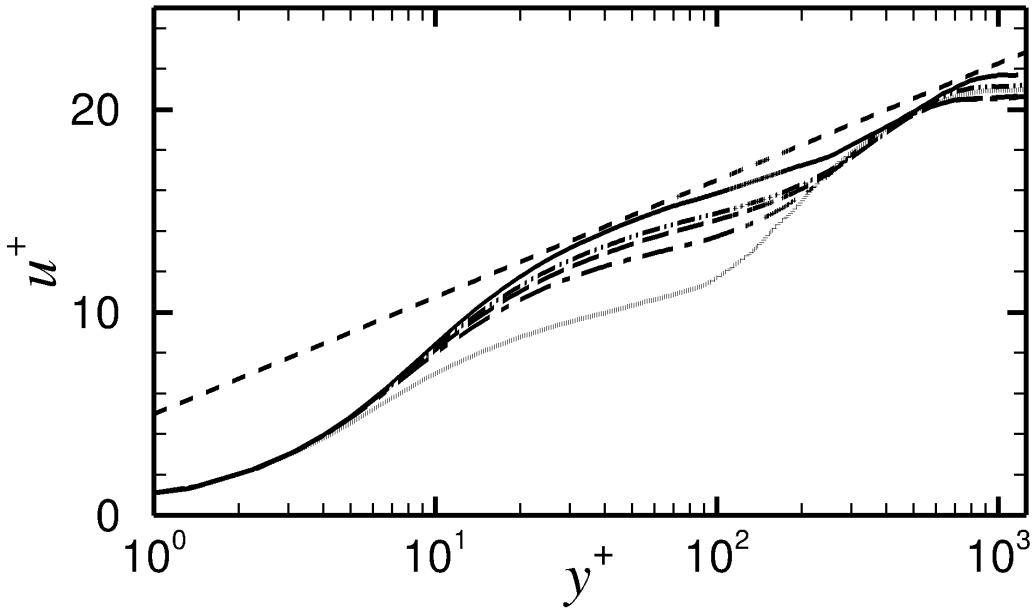

Figure 7. Mean velocity profiles in wall units at the toe of the dune. --- Case 1, $x/H = -9.8$; -·- Case 2, $x/H = -11.2$; — — — Case 3, $x/H = -12.2$; -·-· Case 4, $x/H = -12.8$; —— Case 5, $x/H = -14$. --- Logarithmic law-of-the-wall: $u^+ = \ln y^+/\kappa + 5.0$.

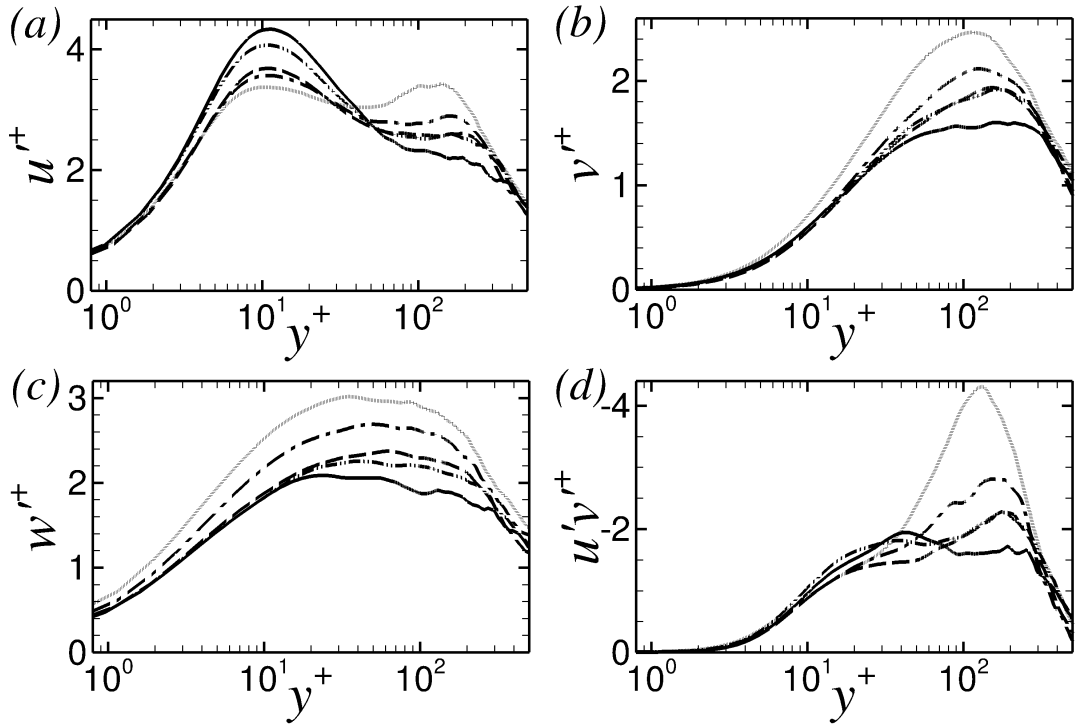

Figure 8. RMS velocity profiles and Reynolds shear stress in wall units at the toe of the dune. ··· Case 1, $x/H = -9.8$; - - - Case 2, $x/H = -11.2$; — — — Case 3, $x/H = -12.2$; - - - - Case 4, $x/H = -12.8$; —— Case 5, $x/H = -14$.

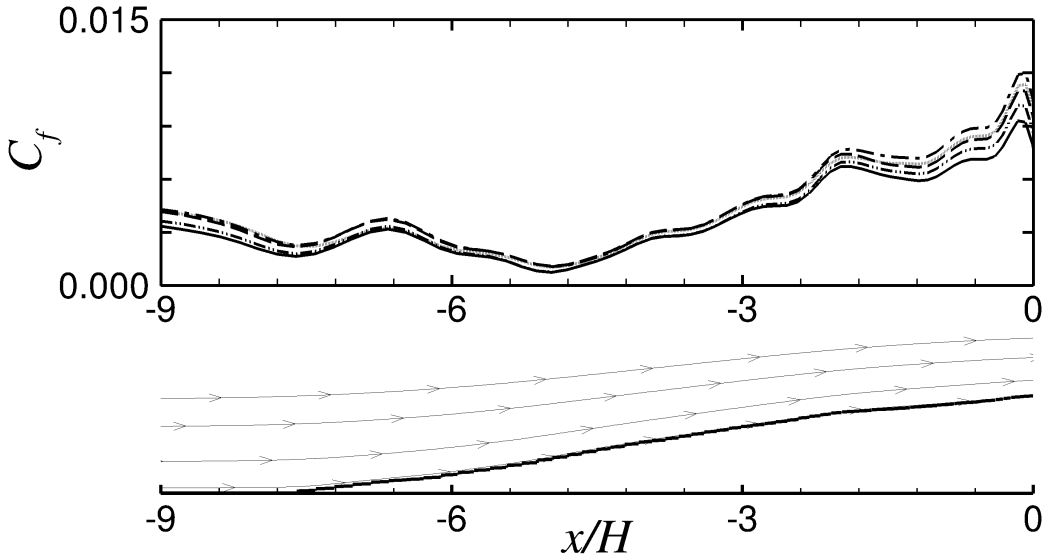

Figure 9. Skin friction coefficient on the stoss side of dunes ($-8.0 \leq x/H \leq 0.0$).

--- Case 1; -·- Case 2; — — — Case 3; -··- Case 4; —— Case 5.

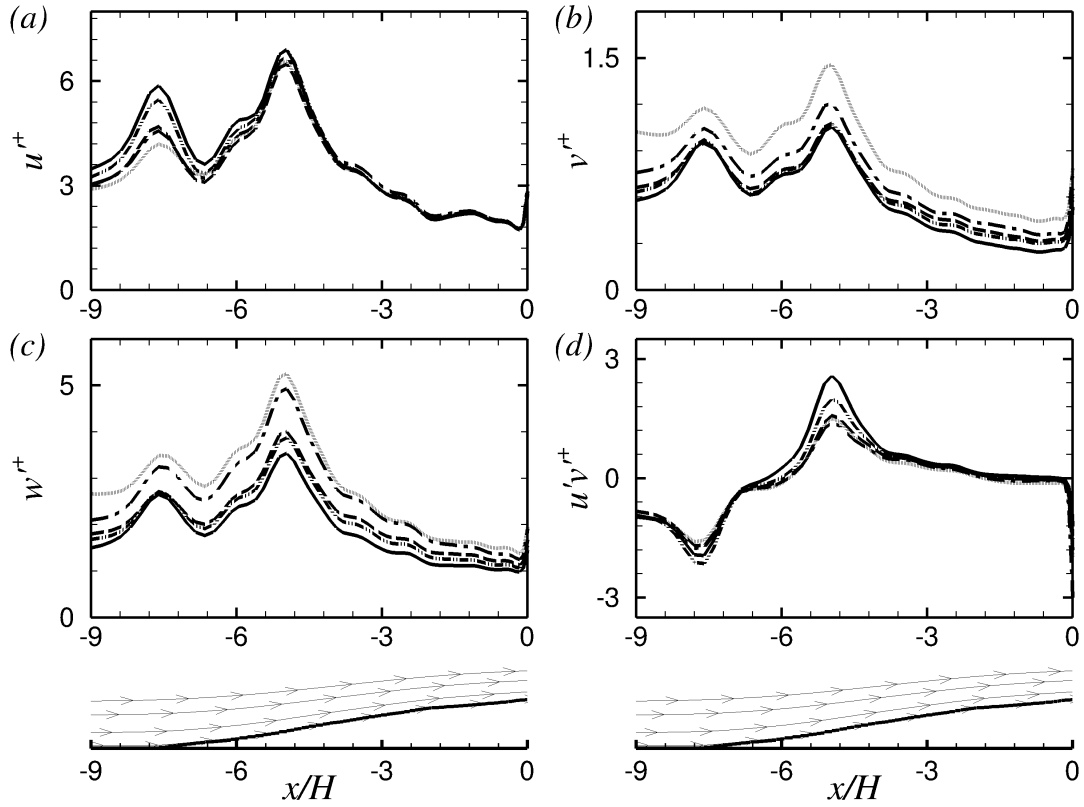

Figure 10. RMS velocity profiles and Reynolds shear stress in wall units; *(a)* u'_{rms}, *(b)* v'_{rms}, *(c)* w'_{rms}, *(d)* $u'v'^{+}$ along the stoss side of dunes on the centerline symmetry plane. --- Case 1; – – – Case 2; ——— Case 3; – – – – Case 4; ——— Case 5.

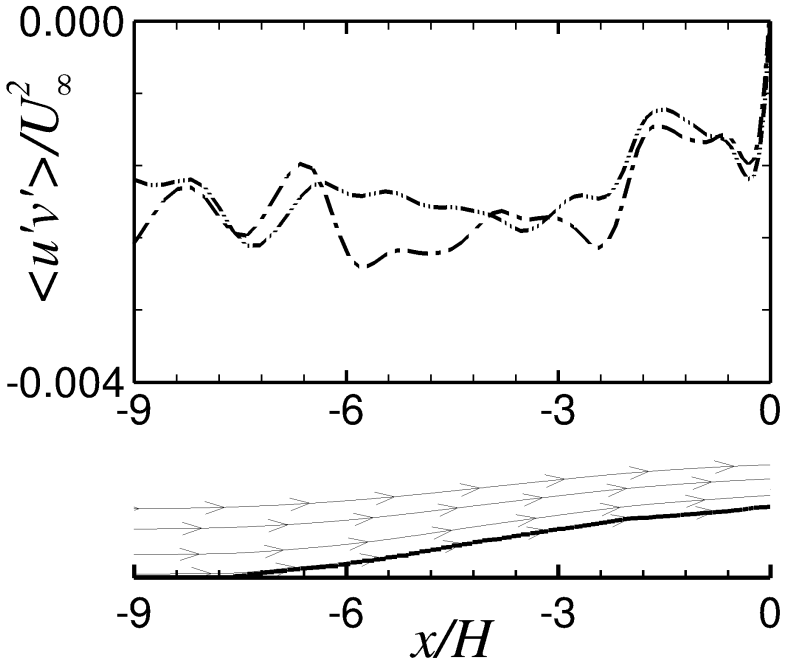

Figure 11. Reynolds shear stress in the parallel- and normal-to-bed coordinate frame along the stoss side of dunes on the centerline symmetry plane. – – – Case 2; – – – – Case 4.

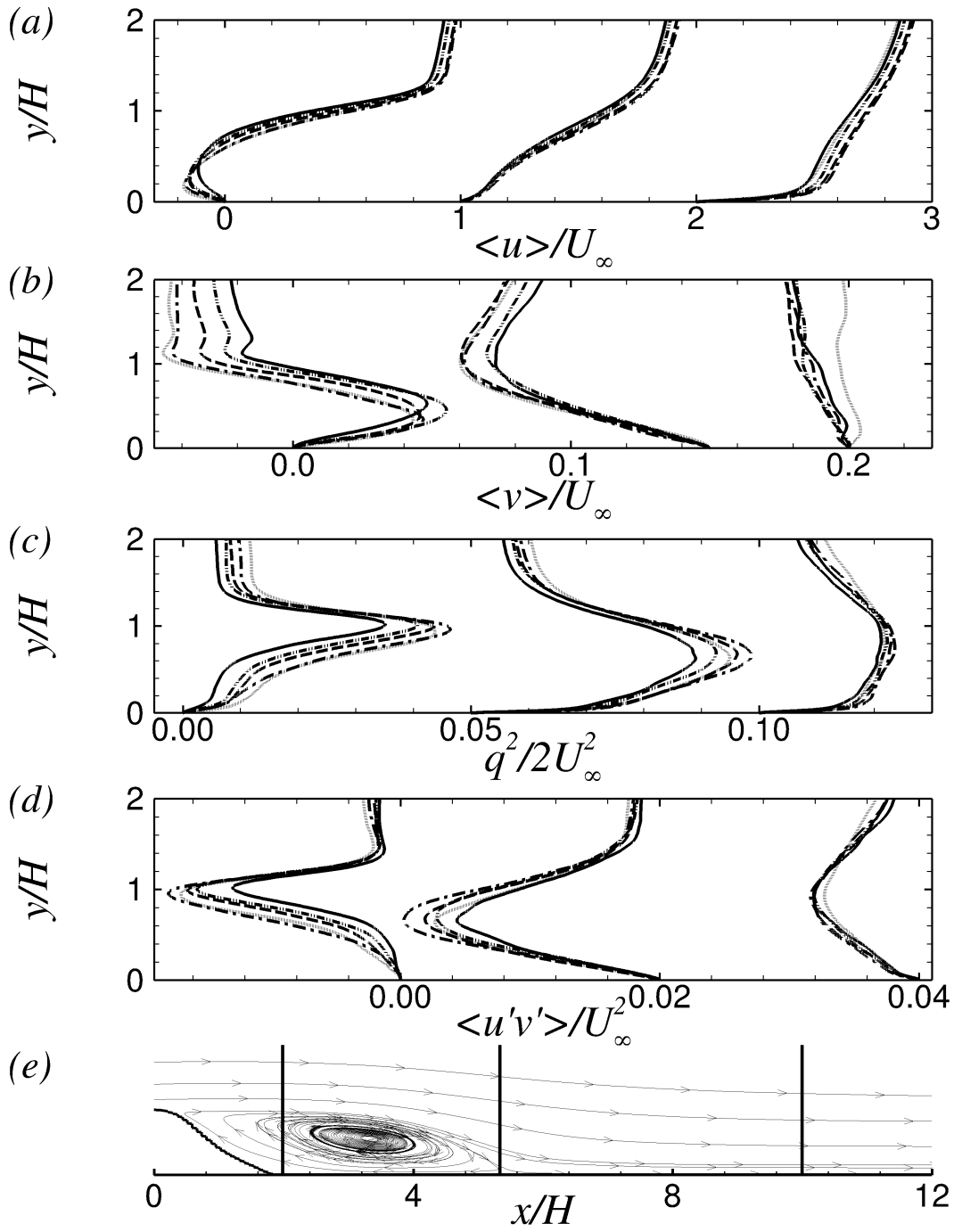

Figure 12. *(a)* $\langle\overline{u}\rangle/U_\infty$, *(b)* $\langle\overline{v}\rangle/U_\infty$, *(c)* $\langle\overline{w}\rangle/U_\infty$, and *(d)* $\langle u'v'\rangle/U_\infty^2$ over three vertical lines at $x/H = 2.0$ passing through the separation zone, $x/H = x_r$ at the reattachment point, and $x/H = 10.0$ downstream of the reattachment point and aligned with the streamwise location of horns. ··· Case 1; – – – Case 2; ——— Case 3; – · – · Case 4; ——— Case 5.

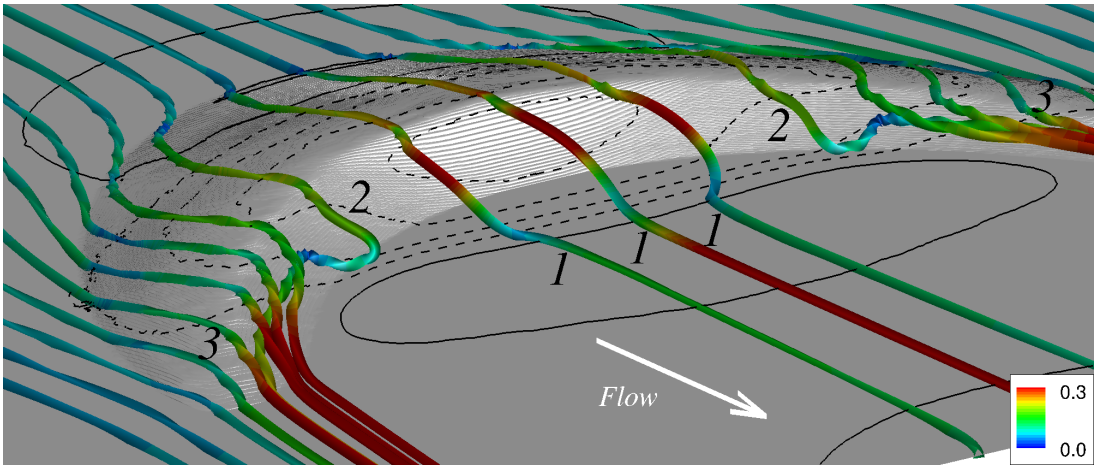

Figure 13. Streamlines close to the bed for the barchan dune of Case 3. Streamlines are colored with the magnitude of the velocity vector. Contour lines of mean pressure are shown on the bed surface; —— $\langle \overline{p} \rangle = 0.0$, --- $\langle \overline{p} \rangle = -0.005 \rho U_\infty^2$.

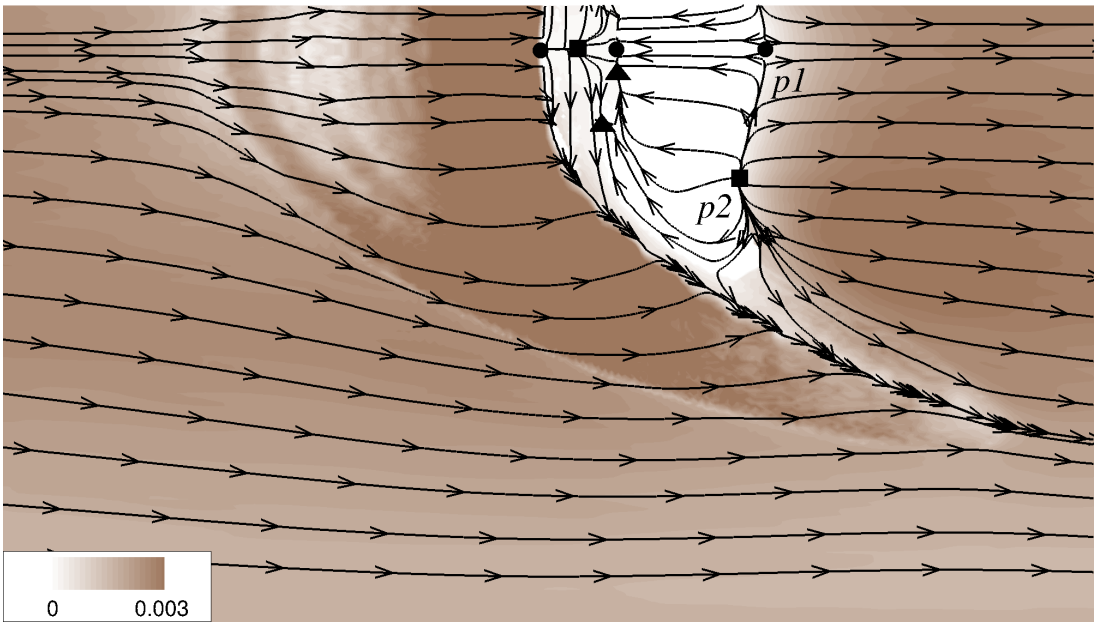

Figure 14. Contours of bed shear-stress, $\tau_w / \rho U_\infty^2$ for Case 3. Streamlines represent the flow direction at the first grid point above the bed surface. ● saddle points of separation; ■ nodal points of attachment; ▲ nodal points of separation

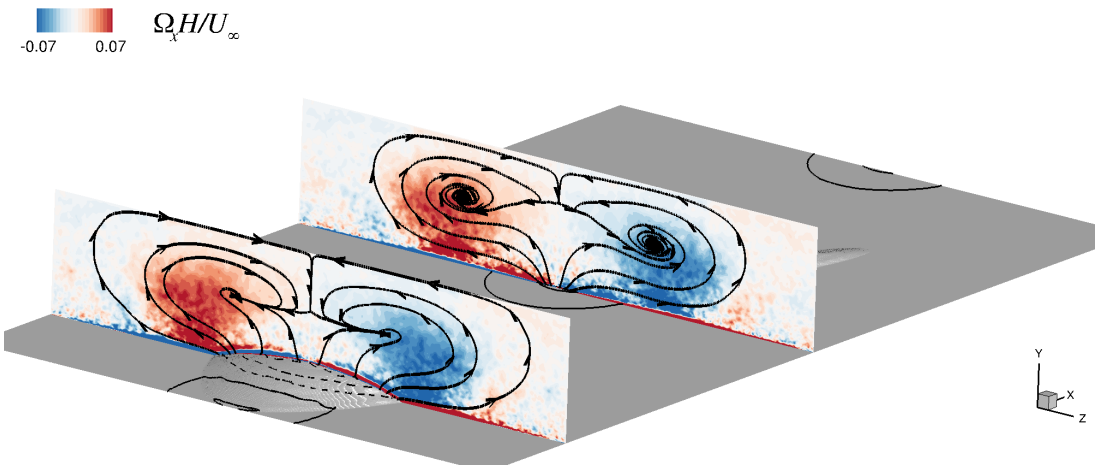

Figure 15. Contours of mean streamwise vorticity, $\Omega_x H/U_\infty$, on two vertical planes across the channel at the crest, $x/H = 0.0$, and at the toe, $x/H = -8.0$, for Case 3. Streamlines tangential to these planes show the secondary flow. Contour lines of the mean pressure are shown on the bed surface; —— $\langle\overline{p}\rangle = 0.0$, --- $\langle\overline{p}\rangle = -0.005\rho U_\infty^2$.

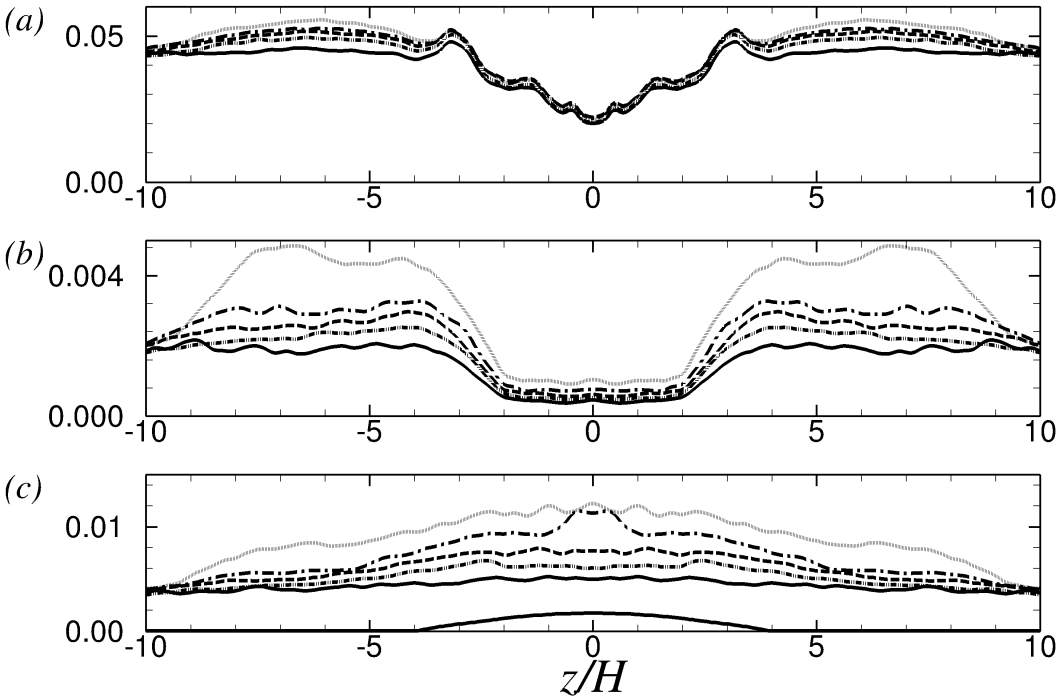

Figure 16. *(a)* u_τ/U_∞, *(b)* $\langle v'v'\rangle/U_\infty^2$, and *(c)* $\langle w'w'\rangle/U_\infty^2$ on the stoss side ($x/H = -5.0$), $0.1H$ above the bed. --- Case 1; -·- Case 2; ——— Case 3; -·-· Case 4; —— Case 5

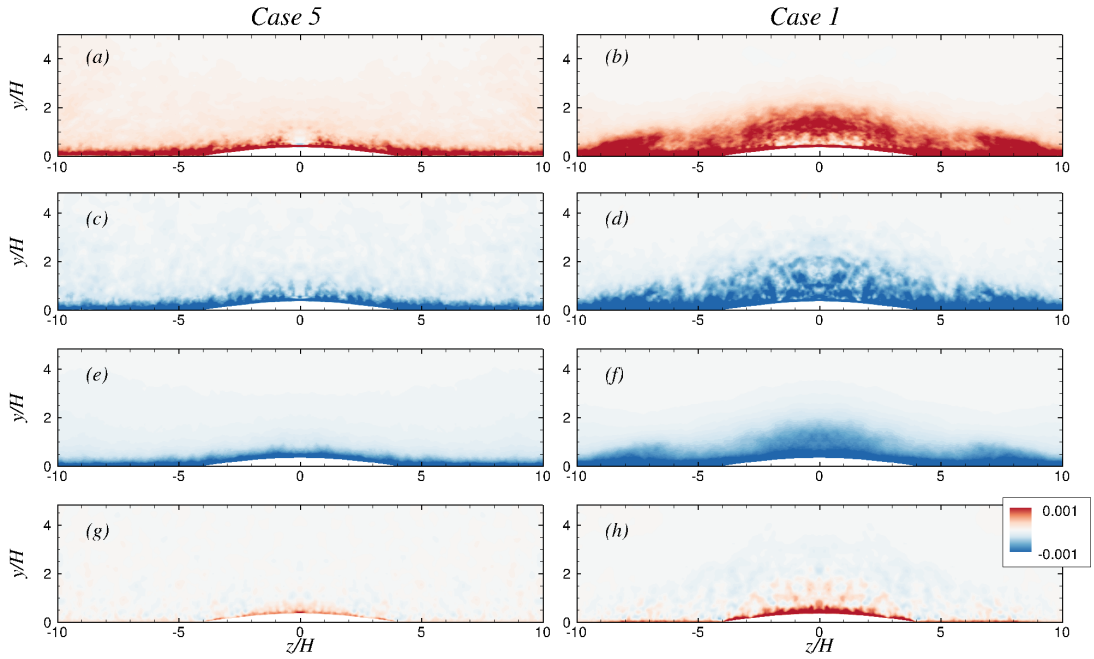

Figure 17. Contours of terms in the turbulent kinetic energy budget at $x/H = -5.0$: *(a,b)* production, $-\langle u_i' u_j' \rangle \frac{\partial \langle \overline{u_i} \rangle}{\partial x_j}$, *(c,d)* mean-flow advection, $-\langle \overline{u_j} \rangle \frac{\partial k}{\partial x_j}$, *(e,f)* dissipation, $-\nu \left\langle \frac{\partial u_i'}{\partial x_j} \frac{\partial u_i'}{\partial x_j} \right\rangle + \left\langle \frac{\partial u_i'}{\partial x_j} \tau_{ij}' \right\rangle$, and *(g,h)* pressure transport, $-\frac{1}{\rho} \left\langle u_i' \frac{\partial p'}{\partial x_i} \right\rangle$. *(a,c,e,g)* Case 5, and *(b,d,f,h)* Case 1.

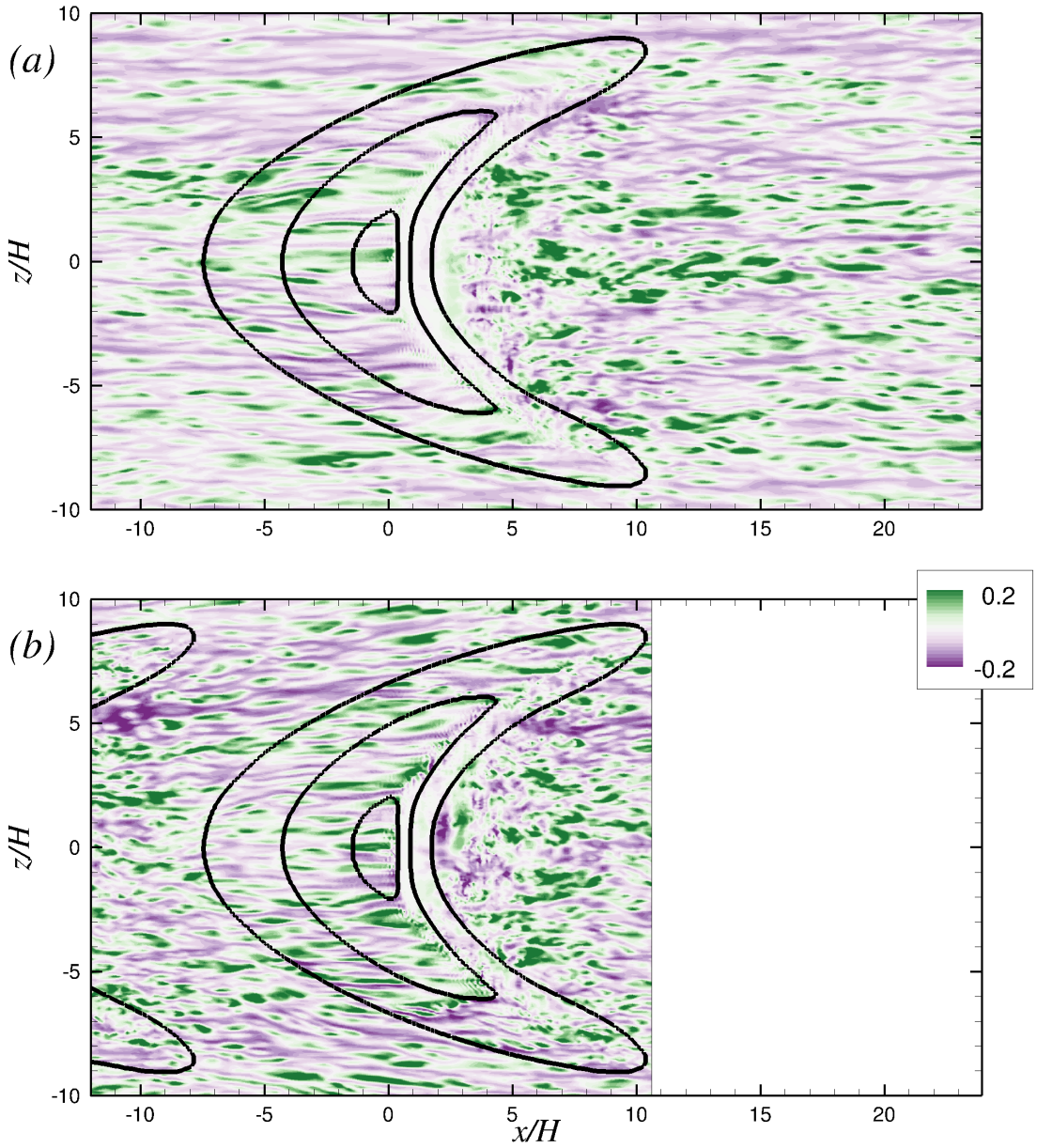

Figure 18. Contours of u' on a plane parallel to the bed surface with a distance $0.025H$ for *(a)* Case 5, and *(b)* Case 1. The lines correspond to the bed levels at $y/H = 0.03$, 0.5, and 0.9.

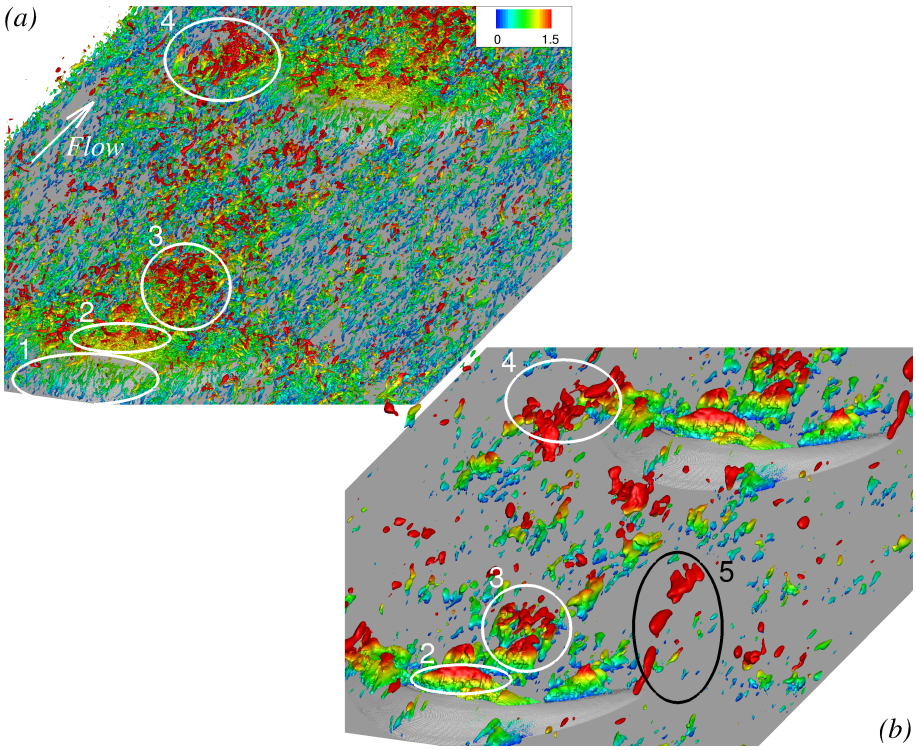

Figure 19. *(a)* Isosurfaces of the second invariant of velocity gradient tensor, $QH^2/U_\infty^2 = 0.35$, and *(b)* isosurfaces of pressure fluctuation, $p'/\rho U_\infty^2 = -0.007$, colored by distance from the bed at $y/H = 0.0$ for Case 5.

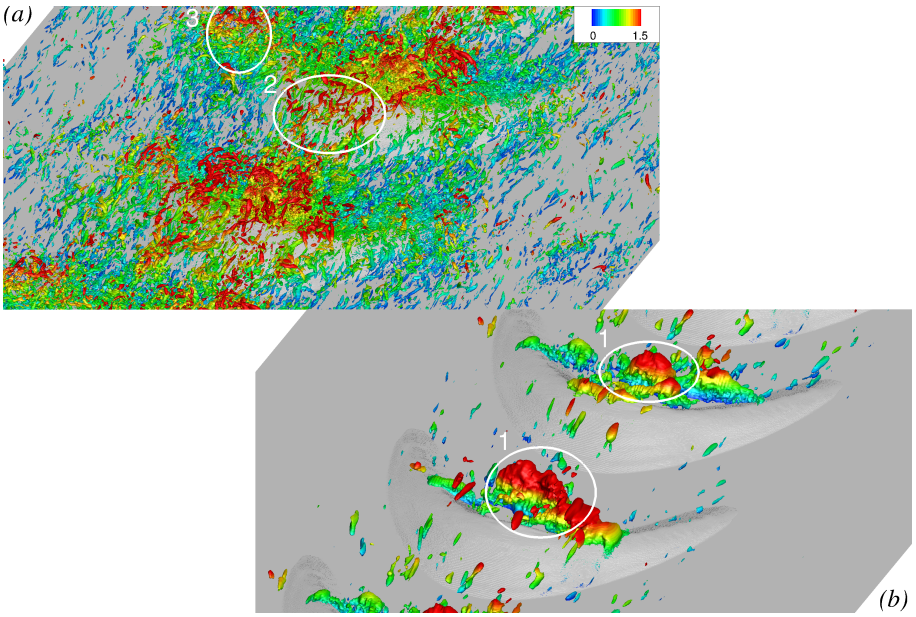

Figure 20. *(a)* Isosurfaces of the second invariant of velocity gradient tensor, $QH^2/U_\infty^2 = 0.70$, and *(b)* isosurfaces of pressure fluctuation, $p'/\rho U_\infty^2 = -0.014$, colored by distance from the bed at $y/H = 0.0$ for Case 1.

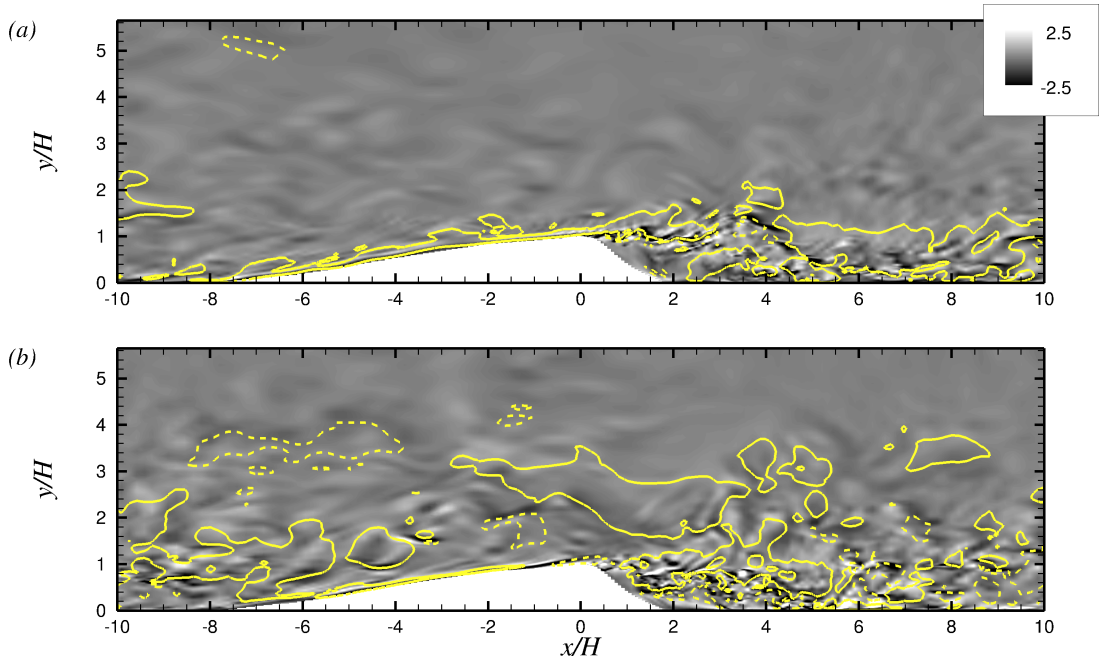

Figure 21. Contours of spanwise vorticity fluctuations, $\omega_z' H/U_\infty$ on the centerline symmetry plane of *(a)* Case 5 and *(b)* Case 1. Solid lines represent $u'/U_\infty = 0.12$, and dashed lines show $u'/U_\infty = -0.12$.